

MHD-Induced Alpha Particle Loss in TFTR

S.J. Zweben, D.S. Darrow, E.D. Fredrickson,
G. Taylor, S. von Goeler, R.B. White

Princeton Plasma Physics Laboratory, P.O. Box 451, Princeton, NJ 08543

Abstract

MHD-induced increases in alpha particle loss to the wall were observed for both coherent modes and transient reconnection events using an array of scintillator detectors near the wall of TFTR. The magnitude of the coherent MHD-induced alpha loss as seen by these detectors was normally comparable to the MHD-quiescent first-orbit or TF ripple loss, but the magnitude of the alpha loss during reconnection events was up to 1000 times higher than this for a short time. Modeling suggest that the coherent MHD loss mechanism will be even less significant for future reactor-scale DT tokamaks due to the smaller ratio of the alpha gyroradius to minor radius.

1. Introduction

The effect of low-frequency magnetohydrodynamic (MHD) activity on the confinement of 3.5 MeV alpha particles is one of the most basic issues in tokamak physics, since it involves the dynamics of single particle orbits in the presence of simple toroidal symmetry-breaking perturbations. This is also a topic of some interest for the development of future DT reactors, since any significant loss of alpha particle confinement could lead to a loss of alpha heating power, or to an unplanned alpha particle heat load on the first wall.

This paper describes measurements of MHD-induced alpha particle loss made during the TFTR DT run using the lost alpha scintillator diagnostic. These observations cover the major types of low frequency MHD activity normally seen in tokamaks, such as coherent low- n “tearing” modes, sawteeth, and disruptions. Since this MHD activity is basically similar between DD and DT discharges [1], the some of the observations are similar to those previously reported for DD fusion products in TFTR [2]. This paper does *not* treat the effects of alpha-particle driven MHD modes such as the toroidal Alfvén eigenmode, which were seen only during DT operation [3]. Therefore the phenomena examined in this paper are specifically “single-particle” MHD-alpha particle interactions, and not the “collective” interactions associated with a large population of alpha particles.

In this sense there were many prior experiments which relate to this subject, since fast ions have been used for many years to heat tokamak plasmas. In general, it has been found that fast ion confinement is not seriously degraded by MHD activity except during strong collective fast ion-driven modes such as beam-driven fishbones or TAEs [4-6]. These measurements were typically made by observing a reduction in the fusion product burnup or a decrease in neutron emission, while the present

experiment describes direct observations of the alpha particle loss to the wall.

The theory of MHD-alpha interactions has been fairly well developed in the past few years, motivated in part by the DT experiments on TFTR, JET, and by the ITER project. Two basic physical interactions have been considered: (a) the effect of coherent low-frequency helical magnetic perturbations on fast ion orbits [7-11], and (b) the effect of sudden magnetic reconnection events on the particle transport [12-14]. These theories take into account for the finite ion gyroradius and orbit size, and in some cases the transit resonances between the ions and the MHD mode.

This paper is organized as follows: Sec. 2 contains experimental details, including a brief review of prior experimental results, Sec. 3 describes the TFTR DT experimental results for alpha particle loss due to coherent MHD and reconnection events, Sec. 4 describes the theoretical modeling of these results, and Sec. 5 discusses the interpretation of these results and their implications for future tokamak experiments.

2. Experimental Details and Previous Results

This section describes the diagnostic set-up and reviews the previous experimental results on MHD-fast ion interactions in tokamaks. A review of the theory and modeling is in Sec. 4

2.1 Lost alpha scintillator diagnostic

All the alpha particle data in the present paper come from the TFTR lost alpha scintillator diagnostic. Since the general design and operation of

this diagnostic have been described previously [15,16], only the details especially relevant to the present experiment are discussed here.

There were four different alpha scintillator detectors arrayed poloidally along the bottom half (ion grad-B drift direction) of the TFTR vessel at one toroidal location. All of these had a similar design, with a 0.1 x 0.2 cm pinhole aperture in front of a 0.1 cm x 0.7 cm slit which dispersed alphas according to their pitch angle and energy, and allowed them to strike a scintillator plate located inside a light-tight box. Three of these four detectors were at poloidal angles of 90°, 60°, and 45° below the outer midplane with their apertures fixed in position ≈ 1 cm radially behind the geometrical shadow of the outer poloidal ring limiters. The fourth detector was 20° below the outer midplane, but radially movable across the outer limiter shadow [17]. Thus the midplane detector aperture position varied from shot-to-shot for the discharges in this paper.

These detectors respond to any fast ions which passed through a thin aluminum foil filter to reach the scintillator plate, so in DD experiments they responded to both 3 MeV protons and 1 MeV tritons. However, in the DT experiments described in this paper the response was almost entirely due to DT alpha particles, so the interpretation of the data is considerably simpler, particularly since the collisionality of 3 MeV protons and 1 MeV tritons are considerably different from each other.

The total light emission from each scintillator for each DT discharge was measured by photomultiplier (PM) tubes and recorded using both a slow and a fast bank of digitizers. The slow bank digitized at up to 20 kHz, while the fast bank digitized at up to 500 kHz, with analog bandwidths of ≈ 20 kHz and ≈ 150 kHz, respectively. The phosphors used for the DT run (P46) had a natural decay time of < 1 μ sec, so were not a limiting factor in the time response of the system. The 2-D scintillator light emission patterns which were used to infer the pitch angle vs. gyroradius

distribution were typically taken with $\approx 1\text{-}10$ msec exposures at a framing rate of ≈ 60 Hz, so were not always able to capture transient MHD events.

Each of these detector signals had a background caused by the neutron/gamma induced fluorescence in the quartz fiberoptic cables used to transfer the scintillator images to the PM tubes and cameras in the shielded basement [15]. This background was proportional to the DT neutron rate and was subtracted out for all the alpha loss signals in this paper. This signal/background ratio was relatively smaller in DT than for the earlier DD fusion products measurements [2], due to the switch to a more robust but much less bright phosphor for DT, and was smaller for the 45° and 60° detectors than for the 90° detector due to the different optical efficiencies (the signal/background in the 20° detector depended strongly on its radial position). The only other significant background was due to hard x-rays occasionally generated by runaway electrons during disruptions, which were not significant for the data discussed in this paper.

2.2 MHD fluctuation diagnostics

The standard TFTR fluctuation diagnostics were used to measure the MHD mode activity described in this paper. The two main diagnostics were the poloidal and toroidal arrays of magnetic pickup (Mirnov) loops on the vessel wall, and the electron cyclotron emission (ECE) measurements of local electron temperature inside the plasma at two toroidal locations. The frequency response of these diagnostics was up to ≈ 200 kHz.

These fluctuation measurements give the frequency spectrum and poloidal and toroidal mode numbers of the internal magnetic perturbations. When analyzed in combination with equilibrium calculations, these two

diagnostics produce the same result for the inferred magnetic island width and location for coherent modes [18]. The analysis of the highly time-dependent magnetic reconnection events is more complicated and uncertain, but some results have been obtained on the internal mode structures of sawteeth and disruptions [19]. High bandwidth neutron flux monitors were also capable of resolving neutron source fluctuations up to ≈ 20 kHz along various chords through the plasma [20].

There was a significant degree of shot-to-shot variability in the MHD activity which made controlled scans of MHD behavior difficult, given the small number of DT discharges which could be made for any experiment. Therefore the data set described in this paper contains representative examples of MHD-induced alpha loss, but not any systematic scans which could have clarified the underlying physical dependences.

2.3 Previous experimental results

The experimental results concerning interactions between fast ions and MHD modes in tokamaks (up to 1994) were reviewed in Ref. 4. The phenomena in that review were divided into “resonant loss”, in which the frequency of the dominant MHD mode matched some characteristic frequency of the fast ion motion, and “non-resonant loss”, in which it did not. The former were mainly associated with collective fast ion, which are not relevant to the data described here.

Previous examples of non-resonant MHD-induced fast ion transport in tokamaks were mainly associated with sawtooth crashes and $m=2$ modes. For example, sawtooth crashes were observed to redistribute beam ions in JET using a neutron camera [21], and coherent $m=2$ modes were observed to cause a reduction in the ^3He burnup in PDX [5]. There were also clear observations of the non-resonant loss of fusion products due to

collective MHD instabilities driven by NBI ions, for example, decreases in the burnup of 0.8 MeV ^3He ions in PDX associated with the fishbone instability in PBX [22] and the TAE instability DIII-D [6].

The effects of MHD activity on DD fusion product loss in TFTR were described and modelled previously [2]. Strong coherent MHD modes were observed to increase the fusion product loss by up to a factor of five above the MHD-quiescent first-orbit loss level in the 90° scintillator detector. Small bursts of fusion product loss were observed at sawtooth crashes, and large bursts just prior to major disruptions. In general, the experimental results for alphas in DT were qualitatively similar to these earlier DD fusion product results, as expected from the fact that the gyroradii of these fusion products are similar (see Sec. 5.1.6).

The effect of kinetic ballooning modes (KBM) on DT alpha loss was reported previously [23]. KBM modes are high-frequency ($f \approx 150$ kHz) and relatively high mode number ($n \approx 6$) fluctuations sometimes observed on the magnetic loops and ECE signals near the beta limit in TFTR. These fluctuations were correlated with a factor-of-two increase in the alpha loss in the 90° scintillator detector, and a numerical orbit model was developed to explain this. A few other examples of MHD-induced alpha loss in TFTR have been described before: the large alpha loss due to a major disruption [16,19], the effect of ELMS on alpha loss [24], and, most recently, the effect of sawteeth on alpha loss in discharges with relatively toroidal field [13].

The only other MHD-induced alpha particle effect seen on TFTR was a sawtooth-induced redistribution of confined alphas as measured by the pellet charge exchange [25] and α -CHERS [26] diagnostics. Although the internal sawtooth-induced redistribution of confined alphas was large, no increased alpha loss was associated with the sawtooth crashes in those $I=2.0$ MA, high toroidal field cases (see Sec. 5.1.5).

3. Experimental Data on MHD-Induced Alpha loss

This section presents experimental data on MHD-induced alpha loss in TFTR DT plasmas as measured by the lost alpha scintillator detectors. In general, there were two classes of MHD instabilities in TFTR: coherent modes (such as tearing modes), which had many oscillation periods and normally reached a nearly steady-state amplitude, and transient reconnection events (such as sawteeth and disruptions), which were intrinsically non-periodic.

Sec. 3.1 gives several examples of the time dependences of the coherent MHD-induced alpha loss, Sec. 3.2 gives examples of the alpha loss during MHD reconnection events, Sec. 3.3 gives data on the pitch angle and gyroradius distributions of these losses, Sec. 3.4 describes the variation of the MHD-induced alpha loss from a database of 21 examples, Sec. 3.5 gives data on the poloidal distributions of these losses, and Sec. 3.6 gives estimates of the total alpha loss fractions, and Sec. 3.7 describes results from a wider database of TFTR DT shots. All of the data in this paper is from NBI-heated DT plasmas with at least one T beam source and without RF heating, since RF can produce fast ion loss which can not be distinguished from alpha loss.

3.1 Time Dependence of for Coherent MHD

Five examples of the coherent MHD-induced alpha loss in NBI-heated TFTR DT discharges are shown in Figs. 1-5. These cases illustrate the wide variety of behavior seen during MHD activity in TFTR. The main parameters for these discharges are summarized in Table 1.

The first example, shown in Fig. 1, was from a normal TFTR DT “supershot” with $I=1.5$ MA, $B=4.9$ Tesla, $R=2.45$ m, and 16 MW of NBI from 3-4 sec (#86289). This discharge had a ≈ 0.1 sec burst of ≈ 1 kHz coherent MHD near the time of peak fusion power and stored energy. This MHD was identified by the external magnetic loops as a mixture of $m/n=2/1$ and $1/1$ components. The MHD-induced alpha loss was seen most clearly in the 20° (“midplane”) scintillator detector, the aperture of which was 2 cm radially inside the geometrical shadow of the outer limiter for this shot. The alpha loss at this detector showed a strong modulation at the frequency of the MHD with up to a $\approx 30\%$ increase in peak alpha loss rate compared with before and after the MHD, and an average increase of 15% in the alpha loss during the period of this MHD.

The second example, shown in Fig. 2, was a low current discharge from a series of H-mode experiments having a current ramp-down prior to NBI [24], with $I=1.0$ MA, $R=2.45$ m, $B=4.9$ Tesla, and 20 MW of NBI (#78607). This case has a series of “fishbone” bursts lasting ≈ 0.2 sec near the time of peak fusion power, with each 10 msec long burst consisting of an $m=1$, $n=1$ mode chirping down from ≈ 3 kHz to 0.3 kHz. The largest effect was seen in 90° detector, where the peak alpha loss increased by up to a factor of two at a fishbone burst, but the average alpha loss over these bursts increased by only $\approx 15\%$.

The third example, shown in Fig. 3, illustrates the response of the three fixed detectors to a coherent low frequency MHD mode previously identified as a “neoclassical tearing mode” [18], in a supershot discharge with high internal inductance [27], with $I=2.3$ MA, $B=5.1$ Tesla, $R=2.52$ m, and 27 MW of NBI from about 3.4-4.1 sec (#92397). This MHD occurred in a 0.1 sec burst during the rise in fusion power, with a very low frequency of ≈ 0.3 kHz and a dominant mode number of $m/n=2/1$. In this case the MHD-induced alpha loss was largest in the 60° detector, where the peak alpha

loss increased by up to a factor of 2 and the average alpha loss increased by $\approx 25\%$.

The fourth example of MHD effects, as shown in Fig. 4, is different from the previous three since it occurred along with a serious degradation of the plasma energy confinement, as seen by the decrease in the DT neutron level at constant NBI power during 2.5-2.8 sec. This discharge had weak magnetic shear (used for TAE instability studies) with $I=1.8$ MA, $R=2.52$ m, $B=5.5$ Tesla with 21 MW of NBI from 2.3-2.95 sec (#104250), and its MHD was dominated by a very low frequency $m/n=3/1$ mode. This mode did *not* cause an increase in the time-averaged alpha loss in the midplane detector, when compared with a similar discharge without any MHD (#104253). However, the alpha loss was strongly in time, as shown at the bottom of the figure, and the peak alpha loss was a factor of two higher than the loss in the similar but MHD-quiescent discharge.

The fifth and final example of coherent MHD-induced loss is illustrated in Fig. 5, which again shows a discharge in which confinement was apparently degraded with MHD, as seen by the decrease in the DT neutron rate at constant NBI power after 3.9 sec (#79369). This was a relatively low power supershot created for an isotope scaling experiment, with $I=1.6$ MA, $B=4.8$ Tesla, $R=2.52$ m, and 15 MW NBI, and with the MHD apparently triggered by something falling into the plasma at ≈ 3.85 sec. Between 4.0-4.5 sec there was a very coherent, relatively high frequency ($f=5$ kHz) $m/n=2/1$ mode, along with an 11 kHz $m/n=3/2$ mode, followed by a major disruption at 5 sec. During the coherent MHD there was a strong modulation in the alpha loss measured at 45° , but very little modulation on the other fixed detectors. The time-averaged alpha loss increased by $\approx 20\%$ and the peak alpha loss increased about a factor of two in the 45° detector during this MHD.

In summary, coherent MHD-induced alpha loss was observed in each of detectors in the lost alpha poloidal array, but its poloidal location varied with the details of the MHD activity and/or discharge conditions. The magnitude of the coherent MHD-induced alpha loss was generally comparable to or less than the MHD-quiescent alpha loss.

3.2 Time Dependence for Magnetic Reconnection Events

Four examples of the time dependence of alpha loss during MHD reconnection events are shown in Figs. 6-9. These cases cover the three main types of reconnection events in TFTR: major disruptions, minor disruptions, and sawteeth. The plasma parameters for these shots are listed in Table 1.

Figure 6 shows alpha loss during a major disruption in a high fusion power gain, lithium-conditioned supershot [28] with $I=2.3$ MA, $B=5.5$ Tesla, $R=2.52$ m, with 15 MW of NBI (#83546). The disruption coincided with a sudden increase in MHD activity at about 4.733 sec. The peak alpha loss in the 90° detector increased by over a factor of ≈ 200 , and the average alpha loss over a 5 msec period increased by a factor of ≈ 30 compared with the MHD-quiescent first-orbit loss before the disruption. It is interesting that this large alpha deconfinement occurred before the plasma current began to decay, similar to other major disruptions [16,19].

Alpha loss during a minor disruption in an experiment done to maximize the DT fusion power is shown in Fig. 7. This case had $I=2.5$ MA, $B=5.1$ Tesla, $R=2.52$ m and 30 MW of NBI, with a peak fusion power of ≈ 7.5 MW (#76773). The alpha loss rate in the 90° detector increased by up to a factor of ≈ 6 within a time of ≤ 100 μ sec, as shown at the bottom of the figure, but the time-averaged alpha loss over a period 5 msec around this time is only $\approx 10\%$ higher than the alpha loss before this event. This type of

instability is less severe than a major disruption, since the plasma current remains, but more severe than a sawtooth crash, since it causes a $\approx 20\%$ drop in the neutron rate. This type of event is seen near the beta limit in many TFTR conditions, including the shot with the TFTR-record fusion power (#80539).

Finally, the effect of sawtooth crashes on alpha loss is shown in Figs. 8 and 9. Fig. 8 shows data from a pair of similar low toroidal field discharges used for TF ripple loss studies [17], with $I=1.4$ MA, $B=3.4$ Tesla, $R=2.52$ m with 8 MW of NBI (#87529/87530). These sawteeth are preceded by a growing ≈ 5 kHz $m/n=1/1$ mode, which had relatively little effect on alpha loss. The crash itself caused a factor to ≈ 2 increase in alpha loss in the 20° detector, as shown at the top of Fig. 8, and a factor of $\approx 3-10$ increase in the 90° detector. However, the time-averaged alpha loss over a 5 msec period around the sawtooth crash was only $<20\%$ higher than the sawtooth-free period. The detailed time evolution of the sawtooth-induced alpha loss varied with each detector, as illustrated at the bottom of Fig. 8. The crash in the central electron temperature is accompanied by a prompt burst in the 90° detector (within 0.1 msec), but the alpha loss seen in the 20° and 60° detectors is delayed 0.1-0.2 msec with respect to this crash.

Fig. 9 shows another case of sawtooth-induced alpha loss, this time for a high toroidal field discharge with $I=1.4$ MA, $B=4.9$ T, $R=2.52$ m and 15 MW of NBI (#79175). This shot had a single large sawtooth near the peak of the DT neutron rate, during which there was a large burst of alpha loss in the 90° and 60° detectors, but relatively little alpha loss in the 45° detectors, as in Fig. 8. Despite these two examples, sawteeth do not normally occur in NBI-heated TFTR discharges, and not all TFTR DT discharges with sawteeth have bursts of loss (see Sec. 5.1.5).

In summary, these examples show that the alpha loss during reconnection events can increase by a factor of over 100 above the MHD-

quiescent level for a period of short time $\approx 0.1-1$ msec. The detailed time structure of the MHD reconnection events and the corresponding alpha loss is complex and not entirely reproducible in detail from shot-to-shot, perhaps due to a varying toroidal localization of the reconnection processes.

3.3 Pitch Angle and Gyroradius Dependences

Data on the pitch angle and gyroradius distributions of the alpha loss was obtained from the 2-D pattern of alpha loss onto the scintillator screens, as measured using a gated intensified video camera. Since the gating pulse width was typically much less than the time between frames (16 msec), only a small fraction of the MHD events were captured on video. A few examples of the pitch and gyroradius distributions of MHD-induced alpha loss are shown in Fig. 10-13.

Fig. 10 compares the pitch and gyroradius distributions measured before, during, and after the coherent MHD activity which was shown in Fig. 1. In this case there is little change in the shapes of these distributions during the MHD, at least averaged over many MHD cycles in this 20° detector. This suggests that the MHD alpha loss mechanism increases, but does not fundamentally change, the MHD-quiescent alpha loss processes [17].

Fig. 11 shows 2-D plots of the pitch vs. gyroradius distributions during the very slow coherent MHD in Fig. 4, where it was possible to resolve the change in these distributions within an MHD oscillation period. In part (a) is the pattern at a time of peak alpha loss, in parts (b) and (c) are patterns at times of minimum alpha loss, and in part (d) is the pattern for a very similar discharge without such MHD activity, which is similar to the time-averaged pattern with MHD in (a). Again, the MHD does not seem to change the basic loss mechanisms in this detector, since the average pitch

vs. gyroradius distributions are not changed, but the alpha loss is clearly strongly modulated and sometimes increased by the MHD. The interpretation of these pitch angle distributions is discussed further in Sec. 5.1.2.

Figure 12 shows the effect of a major disruption on the 2-D patterns of alpha loss to the 20° and 90° detectors, here for a discharge with plasma parameters similar to that of in Fig. 2. The instantaneous alpha loss in the 90° detector increased by a factor of ≈ 1000 in this case, while the alpha loss in the 20° detector increased by a factor of ≈ 10 . The 90° detector shows a large loss of partially thermalized alphas during the disruption, when compared with the pre-disruption pattern, with the peak of the inferred alpha energy spectrum at ≈ 2.5 MeV compared with 3.5 MeV before the disruption. There is a similar but smaller contribution from partially thermalized alphas lost in the 20° detector during disruption. Note that the scintillator light output is linearly proportional to the alpha energy, so these signals are naturally weighted toward the high energy end of the alpha particle energy spectrum.

Finally, Figure 13 shows the effect of a sawtooth crash on the pitch and gyroradius distributions for the case of Fig. 9. The pitch angle distribution in the 90° detector shows a peak near the passing-trapped boundary, as expected from the conversion of passing alphas to trapped alphas [11,13]. The alpha gyroradius distribution does not change significantly during the crash, indicating that the sawtooth-induced alpha loss consists of nearly birth energy alphas.

3.4 Variations in the MHD-Induced Alpha Loss

A set of 21 examples of TFTR discharges with relatively large MHD-induced alpha loss of various types is listed in Table 1. This section will

describe the variation of the relative MHD-induced alpha loss in the 90° detector versus MHD type among this data set. The poloidal dependence, absolute alpha loss fraction, and the wider database are discussed in succeeding sections.

Fig. 14 shows the peak MHD-induced alpha loss rate measured in the 90° scintillator detector during the MHD activity shown listed in Table 1. The horizontal axis is the general classification of the MHD activity for each case, and the vertical scale is peak alpha loss rate normalized by the DT neutron rate at that time. The MHD-quiescent alpha signal level corresponding to the first-orbit loss [16] is subtracted out in all cases, but its relative level is shown separately by the shaded region near the bottom of the figure. The first-orbit alpha loss rate decreases by about a factor of 5 over the plasma current range of $I=1.0$ to 2.7 MA in this data set.

The conclusion from Fig. 14 is that major disruptions caused the largest peak alpha loss rate in the 90° detector, and coherent MHD caused the smallest alpha loss rate. Specifically, the alpha loss rate increased by a factor of ≈ 100 -1000 above the first-orbit loss level during major disruptions, but only by a factor of 0.1-10 during coherent MHD. Minor disruptions and sawtooth crashes showed an increase of 1-100 above the first-orbit loss level. Note that each type of MHD activity has a different time duration (see Sec. 3.6), and that for some of the reconnection cases the data was under-sampled, leading to a systematic underestimate of the peak alpha loss rate.

An attempt was made to relate these peak MHD-induced alpha loss rates with the associated drops in the DT neutron rate, as shown in Fig. 15. The vertical scale is the same as in Fig. 14, but the horizontal scale is the percentage drop in the neutron rate during the duration of the MHD. The cases shown at a “1%” neutron drop had a negligible drop of $\leq 1\%$, while those shown at “100%” drop were associated with major disruptions where there was a drop to zero neutron rate. In between these limits the data falls

along an approximately linear curve, showing at least a qualitative correlation between the amount of MHD-induced alpha loss and the degree to which this MHD affects the reactivity of the discharge.

A more physically meaningful source of variation in the MHD-induced alpha loss is the variation in the size of the local magnetic perturbation, which is related to the local magnetic island width. The MHD-induced perturbations are measured in TFTR using the electron cyclotron emission diagnostic, which provides a radial profile of the electron temperature versus time. A typical example of the effect of a coherent MHD mode on the electron temperature profile is shown in Fig. 16, in which the local radial displacement is ≈ 4 cm in a perturbation which extends from $R=270-320$ cm. The externally measured magnetic fluctuations are useful for determining the mode numbers m/n , but are not useful for characterizing the strength of the internal perturbation, except with detailed analysis of the radial mode structure [23].

A data base of such measured local mode displacements versus the relative MHD-induced alpha loss rate at 90° is shown in Fig. 17. Most large, low frequency coherent MHD modes in TFTR typically had a radial displacement of 2-10 cm, with only a few cases near the upper limit, while high frequency KBM modes typically had a smaller displacement of ≈ 1 cm. Based on the data set of Fig. 17, there was no simple correlation observable between these MHD displacements and the level of MHD-induced alpha loss.

In summary, no single plasma or MHD parameter was found which correlated well with the strength of the MHD-induced alpha loss over this data set. This variability was most likely due to different mode numbers and mode locations of MHD within this database.

3.5 Poloidal Distribution and Estimate of Total Loss Fraction

The poloidal distribution of the measured MHD-induced alpha loss for all the cases in Table 1 is shown in Fig. 18. The vertical scale represents the relative magnitude of the peak MHD-induced alpha loss in each detector, after subtracting out the MHD-quiescent alpha loss level and normalizing by the DT neutron rate (as in Figs. 14, 15 and 17). The relative detector efficiencies are taken into account so that the various poloidal angles and shots can be directly compared with each other. Only the alpha loss levels from the three fixed detectors at 45° , 60° and 90° below the outer midplane are plotted, since the data for the 20° detector depended on the detector radial position (see below).

The poloidal distribution for most of the reconnection events, such as major and minor disruptions and sawtooth crashes, was peaked at the 90° detector, with the remainder slightly peaked at the 60° detector, and with all cases having at least an order-of-magnitude lower signal at the 45° detector. For the coherent MHD modes there is a wider range of behavior, with some cases strongly peaked at the 45° or 60° detector, but most fairly uniform in poloidal angle.

The 20° alpha detector data was not used in Fig. 18, since its radial position varied from shot-to-shot, and it was not inserted for all DT discharges. The effect of this radial variation on the MHD-induced alpha loss seen is shown in Fig. 19, which contains data from the 9 out of 21 cases of Table 1 which had 20° data, plus 5 other cases from a wider data set. There was a clear trend for the ratio of the MHD-induced alpha loss in the 20° detector to increase with respect to that in the 90° detector as the detector aperture was moved inward, which is also similar to the trend seen in the MHD-quiescent level alpha loss seen by the 20° detector [17]. However, even at a fixed radial position there is a variation of at least a factor-of-ten in the

20°/90° MHD-induced alpha loss ratio, depending on the type of discharge and type of MHD activity.

3.6 Total Alpha Loss Fraction

A rough estimate of the total alpha loss fraction due to these MHD-induced alpha loss events is shown in Fig. 20, based on the data set of Table 1. The MHD-induced alpha loss fraction F_{MHD} on the vertical axis of this figure is a rough estimate of the fraction of confined alphas lost to the wall due to MHD, compared with the number of alphas contained in the discharge without such MHD. This is estimated from the available data using the following formulae:

$$F_{\text{MHD}} \approx M f_{\text{fo}} (\tau_{\text{MHD}}/\tau_{\text{s}\alpha})/2 \quad \text{for } \tau_{\text{MHD}} < \tau_{\text{s}\alpha} \quad (1)$$

$$F_{\text{MHD}} \approx M f_{\text{fo}}/2 \quad \text{for } \tau_{\text{MHD}} > \tau_{\text{s}\alpha}$$

where M is the spatially-averaged peak (in time) MHD-induced alpha loss rate multiplier, obtained from the average of the 90°, 60°, and 45° data in the units of Fig. 18, where the first-orbit loss rate was taken to be “1” on this scale (as in Fig. 14). Here f_{fo} is the global first-orbit loss fraction taken from Monte Carlo calculations [16], τ_{MHD} is the duration of the MHD events as listed in Table 1, $\tau_{\text{s}\alpha}$ is the average alpha energy decay time inside the plasma, which is taken to be 0.1 s for all cases, and the factor of two takes into account that the M 's are the peak values in time, and not time averages. In the limit where $\tau_{\text{MHD}}/\tau_{\text{s}\alpha} > 1$, the MHD-induced loss can be calculated as a simple multiplier of the first-orbit loss, based on the measured ratio M of the MHD-induced to MHD-quiescent alpha loss. In the

limit where $\tau_{\text{MHD}}/\tau_{\text{s}\alpha} < 1$, the duration of the MHD-induced loss is normalized to the total alpha population in the discharge, which is integrated over the time $\tau_{\text{s}\alpha}$.

For example, for the major disruption of shot #76778 the spatially-average alpha loss rate from Fig. 18 was $M \approx 24$ times the first-orbit loss rate, the duration time of this disruption was $\tau_{\text{MHD}} \approx 2$ msec, and the calculated first-orbit loss fraction for this discharge at $I=2.5$ MA was $f_{\text{fo}} \approx 2\%$; thus the estimated alpha loss fraction due to this event was $F_{\text{MHD}} \approx 0.4\%$. For the case of the coherent mode #92397 (Fig. 3), the spatially-averaged alpha loss rate was $M=0.7$ during this burst with $\tau_{\text{MHD}} \approx 100$ msec, thus the total estimated MHD-induced alpha loss fraction was $F_{\text{MHD}} \approx 0.8\%$ for a first-orbit loss of $f_{\text{fo}} \approx 2.3\%$.

The implication of Fig. 20 is that the largest MHD-induced alpha loss fraction occurred during major disruptions, when typically $\approx 1-10\%$ of the alphas in the discharge were lost to the wall during the $\approx 0.1-1$ ms just prior to the current quench. The corresponding alpha loss fractions due to minor disruptions or sawtooth crashes were estimated to be in the range $F_{\text{MHD}} \approx 0.01-0.1\%$, and for coherent modes $F_{\text{MHD}} \approx 0.1-10\%$, where the highest levels for coherent MHD-induced alpha loss were only comparable to the first-orbit loss levels. Of course, these results are only order-of-magnitude estimates for the alpha loss fraction for various types of MHD in TFTR, due to the unknown spatial distribution of the MHD-induced alpha loss over regions of the wall which were not directly measured.

3.7 Wider Database

The cases of MHD-induced alpha loss discussed so far were chosen due to their fairly obvious time-dependent alpha loss signals. A search

through the larger database of TFTR DT shots showed that about 20% of the ≈ 300 discharges with T beam injection has some clear time-dependent MHD-induced alpha loss.

A separate database of MHD activity in TFTR discharges was created during a recent study of plasma “rollover” [29]. These discharges tended to have relatively slowly varying coherent MHD activity, which was sometimes correlated with a decrease in reactivity versus time in high powered supershot discharges (“rollover”). A typical example from this data base is shown in Fig. 21 (#79127). Here the MHD activity was a coherent 16 kHz, $m/n=3/2$ mode with perturbation which increased slowly up to $\approx 1\text{-}2$ cm after the peak DT neutron rate. In contrast to most of the examples of Sec. 3.1, there was no modulation of the alpha loss rate as measured in any of the detectors. However, when the alpha loss signal was normalized to the DT neutron rate (as measured by a fast scintillator), the resulting neutron-normalized alpha loss signal (when smoothed to reduce noise), did show a $\approx 25\%$ increase correlated in time with the MHD activity, as shown at the bottom of Fig. 21.

This level of MHD-induced alpha loss is at the low end of the range of data relating perturbation size to MHD-induced alpha loss, as shown in Fig. 17. Nearly all of the ≈ 40 discharges of this type in the rollover database had similar behavior. This increase of alpha loss is most likely due to a gradual broadening of the neutron source profile during the MHD activity, as discussed in Sec. 4.4.

The most difficult type of MHD activity to diagnose is stationary magnetic perturbations (a.k.a. locked modes), which do not rotate and so can not be easily seen in either the Mirnov loops or the ECE temperature profiles [30]. There were several examples of modes which became locked after having been rotating, such as in Figs. 1, 3 and 4, in which the MHD-induced modulation of the alpha loss level stopped at the same time. The

phase of the MHD-induced alpha modulation was variable, such that (to a first approximation) there did not seem to be any difference between the effect of a rotating or stationary mode on the magnitude of the MHD-induced alpha loss.

Finally, there were some examples of MHD reconnection events without a clear MHD-induced alpha loss signal on one or more detectors. An example of this is shown in Fig. 22, in which a sawtooth crash produced a burst of alpha loss in the 90° detector but no visible burst in the 20° detector. Similar behavior was observed in other cases of post-NBI sawteeth studied using the confined alpha diagnostics [25,26]. Evidently the alpha transport to the wall during such reconnection events is sensitive to the details of the internal MHD and variable from shot-to-shot.

4. Theory and Modeling

The theory and modeling of MHD-induced alpha loss is essentially the same as applied previously for DD and D³He fusion products [2,5] and NBI ions [31], since this is a “single-particle” interaction, i.e. independent of the number of fast ions. The difficulty in understanding the present results lies in the complexity of the MHD phenomena and in the incompleteness of the alpha loss measurements.

4.1 Theory for Effect of Coherent Modes on Alphas

The most important parameter in the theory of coherent MHD-alpha interactions is the ratio of the alpha gyroradius to the plasma minor radius ρ_α/a , which is also a measure of the alpha banana width for a given plasma

shape and $q(r)$ profile. In the limit where $\rho_\alpha/a=0$, alpha orbits follow field lines and no alpha loss to the wall will occur (assuming no magnetic reconnection). In the limit when ρ_α/a is large (≥ 0.1), a significant MHD-induced alpha loss to the wall can occur simply due to the MHD-induced distortion of closed alpha drift orbits [5]. In between these limits, stochastic alpha diffusion can occur for both passing and trapped particle orbits [11].

The effect of these modes on alpha particle orbits is most easily understood using a guiding center code with an internal helical magnetic perturbation. In the analysis below, the ORBIT code [32] is used with simplified magnetic perturbations of the form :

$$\delta\mathbf{B} = \nabla \times \alpha\mathbf{B}_0$$

[2]

where \mathbf{B}_0 is the equilibrium field, $\alpha = \sum \alpha_{mn}(r) \sin(m\theta - n\phi)$, and $\alpha_{mn}(r) = \text{const.} \times r^m(a-r)$. This produces a relatively broad perturbation which forms an island structure near the chosen rational mode number. The effect on the alpha orbits comes entirely through the change in the magnetic structure, and not due to a change in the perturbing curvature drifts (which was also treated in the theory of Ref. 11). A single perturbation produces a series of islands in the particle drift surface, due to the coupling between the mode and the $n=0$ orbit shift, which produces stochasticity when these drift islands overlap.

An illustration of a single alpha guiding center orbit in the presence of a very large MHD mode in TFTR is shown in Fig. 23, based on a baseline plasma studied previously [17], with $I=1.4$ MA, $R=2.52$ m, and $B=4.8$ T (with a fairly accurate model for the vacuum fields). In this case a co-going 3.5 MeV alpha in with $\rho_\alpha/a \approx 0.07$ is passing through an $m/n=2/1$ magnetic island with a width of $\Delta \approx 20$ cm, corresponding to a peak magnetic field

perturbation of $\delta B/B_0 \approx 3 \times 10^{-3}$. In this case the alpha particle is lost to the wall in only ≈ 100 toroidal transits (≈ 0.1 msec of real time).

The major radius of the outer midplane crossing point of this orbit, as shown at the bottom of Fig. 23, has both an oscillatory and a random component. The oscillatory motion is a result of the orbit guiding center following the 2/1 perturbed field line, and the random component is the result of a collisionless stochastic diffusion. The pure oscillatory motion of the field line is also shown at the bottom for an ion with zero energy.

It is interesting to compare this result with the approximate analytical threshold for resonance overlap leading to MHD-induced alpha stochastic diffusion, which is analogous to that for TF ripple perturbations [9]:

$$\delta_{\text{MHD}} \xi (\varepsilon/n\pi q)^{3/2} (1/\rho_\alpha q')$$

[3]

where δ_{MHD} is the effective toroidal field “ripple” associated with a low m/n coherent MHD mode, ε is the inverse aspect ratio, n is the toroidal mode number, ρ_α is the toroidal alpha gyroradius, and q and q' are the local magnetic safety factor and its derivative. Because of the $1/R$ dependence of the toroidal field, the radial excursion due to the island causes a modulation of the toroidal field strength, giving an effective TF ripple due to low m/n coherent modes of:

$$\delta_{\text{MHD}} \approx \Delta / a \tag{4}$$

where Δ is the magnetic island width, i.e. the maximum radial excursion of a field line in this mode structure. Thus, for the case illustrated above with

$\varepsilon \approx 0.2$, $n=1$, $\rho_\alpha \approx 6$ cm, $q \approx 2$, and $q' \approx 0.1$ cm⁻¹, the estimated stochastic threshold is at $\delta_{\text{MHD}} \approx .01$ or $\Delta \approx 1$ cm, which is consistent with the strong stochasticity observed at $\Delta \approx 20$ cm in Fig. 23. Note that this stochastic threshold applies to passing as well as trapped particle orbits [12], and there is no stochastic motion for $n=0$ perturbations.

Figure 25 shows the alpha loss regions for this case through a systematic scan of the initial alpha birth radius (along the outer midplane) and initial pitch angle (in units of where 1 is purely co-going and -1 is purely counter-going). All orbits on this grid were run for 1000 toroidal transits, but only those orbits which were lost due to the presence of the $m/n=2/1$ MHD mode are shown by the “X”s. Most of the MHD-induced loss orbits are of the form shown in Fig. 23; namely, nearly co-going orbits born outside $R=300$ cm, which hit the wall just below the outer midplane. The next most numerous MHD-induced loss orbits are born nearly counter-going within the radial range $R=280-300$ cm, and hit the wall just below the inner midplane. Finally, there is a relatively small class of MHD-induced loss orbits with a pitch of -0.2 to -0.5 born relatively near the plasma center at $R \leq 290$ cm, some of which are initially passing but lost across the passing-trapped boundary (see Sec. 4.3), and some of which are fat bananas. Both of these latter types of loss orbits are lost in a fairly broad distribution along the bottom of the vessel.

A Monte Carlo run was made to simulate the effect of this same $2/1$ mode on the confinement of a group of alpha particles born with a random pitch angles and a realistically peaked radial source profile. For this run 3000 alphas were followed for 1000 toroidal transits (it was found from a separate run that over 80% of the eventual alpha loss occurred within 1000 transits). The poloidal and toroidal distributions of alpha loss for this example are shown in Fig. 25. The poloidal distribution is strongly peaked between 0° and 60° below the outer midplane, with relatively little alpha loss

predicted near 90° . The toroidal distribution is fairly strongly modulated with an $n=1$ component, which would imply a fairly strongly modulated alpha loss if the mode were rotating past a fixed detector (the mode in this simulation is stationary).

The total MHD-induced alpha loss fraction for this very large 2/1 mode was 19%, while the total first-orbit loss fraction was 14%. Note that this case has the best available model for the vacuum fields [17], and so represents the closest available approximation to the expected poloidal distribution. The dependence of the alpha loss on the mode amplitude is described below. To a first approximation, the locations of the loss regions and poloidal and toroidal distributions are similar for smaller mode amplitudes.

4.2 Comparison with Coherent Mode Data

The variation of global MHD-induced alpha loss versus the MHD island width and mode number for the $I=1.4$ MA case of Sec. 4.1 is shown at the top of Fig. 26. All these simulations were run for 1000 transits with a stationary mode structure and fixed alpha birth profile (parabolic to the 6.7 power). The overall result is that the calculated MHD-induced alpha loss fraction increases approximately as the square root of the MHD island width (or linearly with the internal magnetic field amplitude) for a given mode number. The modes are all stationary in these simulations ($\omega=0$).

The range of the experimental results for coherent modes is also shown in Fig. 26, based on the results of Fig. 20, which are averaged over the three fixed detectors. The range of the data for the estimated MHD-induced

loss fraction is 0.1-10%, which is within the range of the predictions of these simulations for the measured mode displacements (magnetic island widths) of $\Delta \approx 2\text{-}10$ cm (Fig. 19). However, this comparison has considerable uncertainty due to the range of plasma currents ($I=1.0\text{-}2.3$ MA) and modes numbers in this data base, and also due to the limited spatial resolution in the data, so the agreement shown in Fig. 26 should be considered only qualitative.

A separate attempt was made to model the MHD-induced alpha loss in one specific experimental case; namely, the $I=2.3$ MA discharge of Figs. 3 and 16 with a $\Delta \approx 4$ cm wide, $m/n=2/1$ mode (#92397). The modeling was done similarly to the $I=1.4$ MA example above, except that presence of TF ripple and the real frequency of the mode rotation (≈ 10 kHz) were also taken into account. The comparison between experiment and model is shown in Fig. 27 (this same example was described briefly elsewhere [33]). The calculated global alpha loss increased by only $\approx 10\%$ above the MHD-quiescent loss level for a $\Delta \approx 4$ cm wide $2/1$ island (i.e. from $3.6\pm 0.2\%$ to $4.0\pm 0.2\%$ global loss), while a $\Delta \approx 20$ cm wide $2/1$ island caused about a doubling of the MHD-quiescent loss level. Motivated by the temperature perturbation seen near $q=1$ in this case (Fig. 16), the addition of a $\Delta \approx 4$ cm wide $1/1$ island to the $\Delta \approx 4$ cm wide $2/1$ island increased the global alpha loss to $\approx 5\pm 0.2\%$, i.e. an increase of $\approx 40\%$ above the MHD-quiescent loss level.

The data for this case showed a peak MHD-induced alpha loss level a factor of 2 above the MHD-quiescent level in the 60° detector (Fig. 3), but a time-averaged MHD-induced alpha loss of only $\approx 20\%$ above the MHD-quiescent level for the three fixed detectors. Thus the available data falls into the approximate range predicted by the global modeling for this case.

A striking feature of the experimental data is the nearly 100% modulation of the alpha loss rate to the 60° detector in phase with the mode for this case, as shown in Fig. 3 (and common for the other examples in Sec. 3.1). The simulated toroidal angle dependence of the total alpha loss for a stationary $m/n = 2/1 + 1/1$ mode case is similar to that shown at the bottom of Fig. 25, i.e. with about a 50% modulation in the total alpha loss. This is somewhat less than the observed modulation in the time dependence of the alpha loss at a fixed detector for the actual slowly rotating mode.

Variation of the mode rotation frequency between 0 and 10 kHz did not significantly change either the total MHD-induced alpha loss or its toroidal modulation. This is not surprising, since the alpha particle transit frequency (≈ 1 MHz) and precession drift frequencies (≈ 300 kHz) are much higher than the mode frequency (≈ 1 kHz), so the mode rotation does not resonate with the alpha particle orbits (see Sec. 5.1.4).

4.3 Effect of Magnetic Reconnection on Alphas

The theory and modeling of Sec. 4.2 is not sufficient to evaluate the effects of magnetic reconnection on alpha loss, since the mode structure is very complex and the timescales are short enough so that the effects of induced electric fields can come into play in the orbit dynamics. A detailed study of sawtooth-induced reconnection on alpha particle loss in TFTR is described elsewhere [13].

For the sake of a qualitative understanding of the data, a simple model can be described based on the observation that the sawtooth-induced loss often occurs at the passing-trapped boundary (e.g. Fig. 13). Loss across the passing-trapped boundary can come from radial diffusion at a fixed pitch angle and energy [34], as illustrated at the top of Fig. 28 using the generic $I=1.4$ MA, 20 cm $2/1$ island case. The location of this loss orbit is

shown by point A in the map at the bottom of Fig. 28. The maximum possible loss across this passing-trapped boundary occurs when all the alphas confined radially inside the shaded region to the left of A (in Fig. 28b) move outward and across the point labeled A, whereby they are lost near the bottom of the vessel. An analogous loss occurs just below the outer midplane at point B, and just below the inner midplane at C in Fig. 28.

This maximum ratio of the local reconnection-induced alpha loss rate R_{recon} to the first-orbit loss rate R_{fo} is therefore roughly:

$$R_{\text{recon}}/R_{\text{fo}} \approx (\langle S_{\alpha} \rangle_{\text{in}} / \langle S_{\alpha} \rangle_{\text{out}}) (\tau_{\text{s}\alpha} / \tau_{\text{recon}}) \quad [5]$$

where τ_{recon} is the time over which this reconnection-induced radial transport occurs, $\tau_{\text{s}\alpha}$ is the time over which confined alphas slow-down in the core region, and $\langle S_{\alpha} \rangle_{\text{in}}$ and $\langle S_{\alpha} \rangle_{\text{out}}$ are the volume-averaged alpha source rates in the interior confined region, such as the shaded region to the left of A, and the exterior first-orbit loss region to the right of point A, respectively.

For example, in the sawtooth-induced loss case of Fig. 8, $\tau_{\text{s}\alpha}/\tau_{\text{recon}} \approx 0.1 \text{ sec}/0.1 \text{ msec} \approx 1000$, and $\langle S_{\alpha} \rangle_{\text{in}} / \langle S_{\alpha} \rangle_{\text{out}} \approx 1$ at $I=1.4 \text{ MA}$ [34], therefore the maximum possible sawtooth-induced loss rate should be ≈ 1000 times the first-orbit loss rate to this detector. The fact that the observed increase is only a factor of ≈ 10 in this case could imply that only $\approx 10\%$ of the alphas radially within point A, most likely those just radially inside point A, were transported across the passing-trapped boundary during this sawtooth. This upper limit is similar to the upper limit observed during major disruptions, which would most likely cause most of the alphas inside point A to be lost across the passing-trapped boundary. This is consistent with the presence of partially thermalized alphas in the gyroradius distribution observed at the bottom of the vessel during a major disruption (Fig. 12).

This simple model can at least qualitatively explain the large increases in alpha loss seen during reconnection events. However, it ignores the effect of the induced electric fields on the alpha transport, which can change the energy and magnetic moment when the reconnection timescale is comparable to the alpha transit timescale, as is the case for fast reconnection events [12-14].

4.4 Effect of Neutron Profile Variations

All of the preceding modeling assumed that the alpha source profile was constant during the MHD activity. However, it was previously shown that there can be $\approx 10\text{-}20\%$ fluctuations in the local neutron source profile associated with large coherent MHD activity in TFTR discharges [20]. Also, there is sometimes a gradual broadening of the neutron source profile associated with confinement changes due to these MHD modes. Ideally, these local alpha source rate variations should be taken into account in the analysis of the MHD-induced alpha loss for the coherent MHD cases, even though the global alpha loss due does not change or significantly fluctuate in most of these cases.

The effect of a modulated alpha source profile on the calculated alpha loss can be visualized by examining the trajectory of a typical MHD-induced alpha loss orbit in Fig. 23. This alpha orbit makes ≈ 100 passes through the region of the $2/1$ mode before it is lost, but its toroidal phase is quickly randomized with respect to the phase of the mode (otherwise it would not undergo stochastic diffusion). Since alphas are born along the whole length of trajectories such as this, it is highly unlikely that any net modulation of the alpha loss to the wall would be caused by a spatial modulation of the alpha source profile. Thus the fluctuations of the alpha loss signal in phase with the MHD modes can not be attributed to fluctuations in the alpha source profile.

However, a slow broadening of the alpha source profile due to MHD activity will cause an increase in the alpha loss simply due to the increase in the number of alphas born on prompt loss orbits. For example, the measured FWHM of the neutron source profile for the case of Fig. 21 increases from 47 cm to 55 cm during the time of the MHD activity from 4.0-4.7 sec, when the alpha loss to the 90° detector increases by $\approx 25\%$. The calculated first-orbit loss to this detector increases by $\approx 35\%$ due to this change; thus this increase in alpha loss can be entirely attributed to the source broadening, and not to direct MHD-induced alpha loss.

The increases in alpha loss such as those illustrated in Figs. 1-5 are most likely not dominated by variations in the neutron source profile, since these MHD-induced losses were modulated at the MHD frequency and were variable from detector-to-detector. The increases due to reconnection phenomena such as illustrated in Figs. 6-10 were too large to be dominated by neutron profile changes, since the neutron rate most likely decreases across the whole profile during these phenomena.

5. Discussion

This paper described measurements and modeling of MHD-induced alpha loss in TFTR DT plasmas. Normal coherent low m/n MHD activity caused the alpha loss to increase by an amount comparable to the MHD-quiescent alpha loss level. However, transient magnetic reconnection events such as sawteeth and disruptions caused the alpha loss level to increase by up to a factor of 10-1000 above the MHD-quiescent loss level, but only for $\approx 0.1-1$ msec. The net result was that such MHD activity caused only a relatively small fractional alpha particle loss, roughly estimated to be in the range 0.1-10% of the confined alpha population (Fig. 20).

There was at least a qualitative agreement between the modeling of Sec. 4 and the data on MHD-induced alpha loss described in Sec. 3. The best example of this comparison was done for the specific $I=2.3$ MA coherent mode case summarized in Fig. 27, where the measured and modeled MHD-induced alpha loss levels were both in the range $\approx 20-50\%$ above the MHD-quiescent alpha loss levels. The modeling of the reconnection-induced alpha loss was only qualitative, although a more sophisticated model has been applied to the sawtooth data elsewhere [13].

5.1 Comparison of Experiment and Theory

This section describes further connections between experiment and theory, some of which were not resolved by this experiment. Potential improvements in the experimental and modeling techniques are described in the next section.

5.1.1 Modulation due to Coherent Modes

The observed modulation of the detected alpha loss signals at the frequency of the coherent MHD modes (≤ 10 kHz) was explained in part by the toroidal variation of the alpha loss to the wall seen in the simulation results, such as in Fig. 25. The absence of an explicit frequency dependence of the magnitude of the MHD-induced alpha loss in this frequency range is also consistent with the modeling, based on the relatively small mode frequency compared with the alpha particle transit and precession frequencies.

The MHD-induced alpha loss seen during coherent modes, such as shown Figs. 1-5 and Fig. 22, did not show any clear decrease with time during the mode activity, suggesting that the MHD was not causing a net depletion of the reservoir of confined alphas which provided the source for

this MHD-induced alpha loss. This is consistent with the inference of Fig. 20 that there is a relatively small fractional loss associated with these modes. Since the MHD-induced alpha loss process is much faster than the alpha thermalization time for alphas born at any given pitch angle and radius, taking typically ≈ 1 msec in the Monte Carlo code runs, it is possible that the MHD-induced alpha loss is limited by the local alpha source at the birth energy. This is also perhaps the explanation for the apparent absence of low-energy alpha loss associated with coherent MHD, as seen in Figs. 10 and 11.

In a few cases the MHD-induced modulation of the alpha loss in the 20° or 45° detectors was so large that, surprisingly, the instantaneous signal actually went *below* the MHD-quiescent level (e.g. in Figs. 4 and 5). This could occur if the MHD-induced radially inward oscillation of the alpha orbits entering the detector is instantaneously larger than the normal MHD-quiescent radially outward alpha motion (e.g. due to ripple diffusion). For the case of Fig. 4, where the MHD mode amplitude and frequency were $\Delta \approx 10$ cm and ≈ 100 Hz, such a negative modulation should only occur when the MHD-quiescent alpha diffusion rate is roughly $D_\alpha < \Delta^2 \omega_{\text{MHD}} \approx 10^4$ cm/sec. However, this condition is *not* satisfied by the relatively fast stochastic TF ripple diffusion process near the outer wall [17], but would be satisfied if this detector was sampling the confined alpha population (see Sec. 5.1.2). Such a negative modulation is not expected when the MHD-quiescent alpha loss is dominated by the very fast first-orbit loss process, which is consistent with the absence of such a negative modulation in 90° and 60° detector signals.

5.1.2 Pitch Angle Distributions

There were relatively few measurements of the pitch angle of the MHD-induced alpha loss, since good pitch resolution could only be obtained using the relatively slow 2-D imaging camera (see Sec. 3.3). The clearest

observations for coherent modes showed no systematic change in the time-averaged pitch angle spectrum in the 20° detector during MHD (Figs. 10 and 11), while for reconnection-induced loss the pitch was generally near the passing-trapped boundary in the 90° detector (Fig. 13).

For the movable 20° detector, alpha loss near a pitch of $\approx 60^\circ$ corresponds to TF ripple-induced loss with a typical step size of a few cm per transit, while the loss at a pitch of $\approx 50^\circ$ corresponds to collection of confined passing alphas [17], which occurs when the aperture is in well past the limiter boundary (as it is for the case of Fig. 4). Given the rough estimates concerning modulation of the alpha loss at the end of Sec. 5.1.1, one would expect that the non-diffusing component detected near 50° would be strongly modulated by the mode, while the TF ripple diffusion near 60° would not. However, the data of Fig. 11 shows that the peak loss occurs at a average pitch angle of $\approx 55^\circ$, and the lowest level of loss occurs both for 50° and 60°. Therefore this pitch angle variation is not understood.

The observations of passing-trapped boundary loss during sawtooth reconnection events, such as illustrated in Figs. 12(b) and 13, was at least qualitatively explained by the reconnection-based model discussed in Sec. 4.3 (Fig. 28). However, the pitch angle of the alpha loss measured in the 90° detector during the disruption shown in Fig. 12 was well below the pitch angle of the passing-trapped boundary, perhaps due to a change in the $q(r)$ profile during the disruption.

5.1.3 Poloidal Distributions

The poloidal distributions of MHD-induced alpha loss should in theory depend on the assumed ρ_α/a , i.e. on the plasma current for a fixed geometry, which determines the poloidal angle at which the marginally confined alpha orbits intersect the wall. In general, the calculated poloidal distributions of MHD-induced alpha loss become more peaked toward the

vessel bottom with increasing current, as shown at the top Fig. 29 (compare with Fig. 25 at $I=1.4$ MA).

The measured poloidal distributions of coherent MHD-induced alpha loss shown in Fig. 18 did have a significant variability. However, there was no simple correlation with the trend expected from the modeling shown at the top of Fig. 29; namely, for the MHD-induced alpha loss distribution to be more peaked toward the 90° detector location for higher plasma currents. This is most likely due to the sensitivity of the expected poloidal distribution to the vacuum fields, and the considerable variation of the vacuum fields for this data set with varying major radii.

The poloidal distribution observed for the reconnection events shown in Fig. 18 were generally peaked at the bottom of the vessel. This is apparently consistent with the model of Ref. 13, and is approximately consistent with the calculations of the MH3D code for a major disruption (#76778).

The general increase of the MHD-induced alpha loss in the 20° detector as its aperture is moved inward, as shown in Fig. 19, is most likely due to the effect of limiter shadowing on the diffusive loss near the outer midplane [17]. In principle, a radial profile of the MHD-induced alpha loss for a given MHD mode could be used to infer the local radial step size per transit; however, there is insufficient MHD-induced alpha loss data for this purpose.

5.1.4 Kinetic Ballooning Mode

The data set of Table 1 contained two examples of kinetic ballooning mode activity (KBM), one of which (#77309) was used in a previous analysis of MHD-induced alpha loss in TFTR [23]. The internal displacement for these high- n ($m/n \approx 8/6$) modes was relatively small (≈ 1 cm), but they had

much higher frequency of ≈ 150 kHz, and so could resonate with some of the alpha particle orbits. Note that these modes were not driven by the alpha particle population, since very similar modes existed in similar D-only plasmas.

The calculations of the alpha orbit loss in Ref. 23 are similar to those in Sec. 4.2, except for the higher mode number and much higher frequency of the mode rotation. The mechanism for alpha loss is basically the same as described in Sec. 4.3; namely, conversion of counter-passing confined alphas near the plasma center to trapped alphas lost to the vessel bottom. However, the alphas in the KBM case can satisfy the resonance condition for energy exchange between the MHD mode and alpha particle is:

$$\omega_{\text{MHD}} \approx (m/q - n) \omega_t \quad [6]$$

where ω_{MHD} is the mode frequency in the plasma frame and ω_t is the alpha particle transit frequency $\omega_t \approx v_\alpha/R \approx 4 \times 10^6 \text{ sec}^{-1}$. Thus the resonant region is significant for the KBM with $\omega_{\text{MHD}} \approx 10^6 \text{ sec}^{-1}$ and not for low frequency modes. The random energy exchange increases the effective radial step size of the resonant alpha orbit near the passing-trapped boundary, and so increases their effective loss rate across the passing-trapped boundary.

5.1.5 Absence of MHD-Induced Loss

There were several cases in which the normal sawtooth-induced alpha loss such as shown in Figs. 8 and 9 did not occur at all, or was absent in one or more of the detectors, as shown in Fig. 22. This was usually associated with sawteeth which occurred after the turn-off of NBI, such as during the experiments done to measure the effect of sawteeth on confined alphas [25,26]. This might be due to the sensitivity of the reconnection-induced alpha loss to the location of the passing-trapped boundary with

respect to the reconnection region, as illustrated in Fig. 28. For example, if the $q=1$ surface at which the sawtooth-induced reconnection occurs lies outside the radius of the passing-trapped boundary for a given detector, it will become insensitive to the reconnection-induced radial transport [13].

5.1.6 Relation of DT to DD results in TFTR

As stated earlier, the qualitative features of the MHD-induced alpha loss were similar to those observed earlier for DD fusion product loss in D-only TFTR plasmas [2]. This is not surprising since this is a single-particle interaction, and the 1 MeV tritons and 3 MeV protons ions in D-only plasmas have a similar ρ_α/a to DT alphas.

However, the magnitude of the MHD-induced DD fusion product loss appears to be larger relative to the first-orbit loss than for DT alphas, e.g. it was up to a factor-of-four above the first-orbit loss at $I=1.6$ MA in the 90° detector. The most likely explanation is the low thermalization rate for 1 MeV tritons, which is typically ≈ 3 times smaller than for 3 MeV protons or 3.5 MeV alphas ($\propto M/Z^2$). Thus the confined fusion product population which is susceptible by MHD-induced loss is about 3 times larger for tritons relative to its first-orbit loss at the same plasma current. It is also possible that the larger database for D-only plasmas contained MHD activity which was larger than that contained in the DT database.

5.2 Potential Improvements

A major limitation of this experiment was the absence of systematic scans of the MHD behavior, due in part to the limited number of DT discharges and in part due to the intrinsic irreproducibility of these MHD phenomena. The resulting database shown in Table 1 contained a wide variety of discharges, but no systematic variation of any specific type of

MHD activity. This could be improved through a carefully controlled experiment such as the of $q(r)$ scan for measuring the TF ripple loss [17].

The major alpha diagnostic limitations were the sparse spatial coverage and the relatively low signal-to-background level for the scintillators detectors used for DT. The spatial coverage could potentially be improved with detectors near the inboard midplane, but these were not possible in TFTR since the plasmas were limited on the inboard wall. The signal-to-background level for coherent MHD-induced alpha loss was often less than one due to the dim (but rugged) scintillator for DT; much more detail of the time dependence of the alpha loss was seen using a brighter scintillator in DD plasmas [2].

The main limitations in the modeling of these experiments were in the knowledge of the internal structure of the MHD perturbations and of the external vacuum magnetic fields. For this experiment the MHD island widths were determined from the fluctuations in the electron temperature profile, and the MHD mode numbers from external magnetic fluctuation measurements. This was sufficient for an approximate modeling such as described in Sec. 4.2; however, the detailed radial structure of the modes was not well matched, particularly in the cases where multiple modes existed at the same time. The lack of knowledge of the vacuum magnetic fields made it difficult to determine the poloidal distribution of the MHD-induced loss, and therefore difficult to compare with specific detector results.

The ORBIT code used for modeling of the coherent mode effects was limited by available computer speeds to runs with about 5000 particles for 1000 toroidal transits. Ideally, the time dependence of the MHD and the full collisional slowing down process should be modeled for an improved comparison with the data, but this would require a substantially faster code. The complexity of magnetic reconnection phenomena most likely requires a

simplified theoretically-based simulation [13]. Ultimately, a 3-D nonlinear MHD code such as MH3D [35] could self-consistently model both the time evolution of the MHD and the associated alpha loss.

5.3 Reactor Relevance

It was shown in Fig. 29 (see Sec. 5.1.3) that the coherent MHD-induced alpha loss decreases with decreasing ρ_α/a as the alpha orbits become more closely aligned with the magnetic field lines. According to the estimate of Fig. 29, at a reactor-relevant level of $\rho_\alpha/a \approx .01$ even a very large 2/1 island should cause only a $\leq 1\%$ global alpha loss (for TFTR-like geometry). This would have a negligible effect on alpha heating, although detailed calculations in realistic geometry should be done to assess the wall loading implications of this alpha loss in reactor, as were done for TF ripple loss [36].

The effects of reconnection on alpha loss will not scale simply with ρ_α/a , but may depend upon the details of the reconnection process in time and space. However, even if a large fraction of the alphas were lost during a sawtooth crash in a reactor, the plasma would most likely re-heat before the thermal energy was lost, unless the period of the sawteeth was comparable to the energy confinement time [36]. Thus these MHD perturbations do not seem to be particularly dangerous for alpha loss in a reactor.

Major disruptions caused the largest alpha loss fraction in TFTR, and an analogous loss of 10% of the confined alphas in a reactor could potentially damage the first wall. However, the confined alphas might be thermalized during the thermal quench phase of the disruption before they are lost due to MHD, since the electron temperature might reach as low as

100 eV. For example the alpha thermalization time at 10^{14} cm^{-3} at 100 eV is only $\approx 100 \text{ } \mu\text{sec}$, so this alpha thermalization might be present in the TFTR disruptions.

The most likely cause of MHD-induced alpha loss in reactors would be high frequency MHD modes which can resonate with the alpha transit or bounce frequency. If these do not occur, then MHD-induced alpha loss will probably not be a serious problem for a tokamak reactor.

Acknowledgments: We thank C.E. Bush, D.W. Johnson, R. Fisher, Y. Kolesnichenko, H.E. Mynick, W. Park, I. Semenov, J.D. Strachan, and H. Takahashi for their helpful discussions concerning the material in this paper, and M. Bell, H.P. Furth, D. Meade, R. Hawryluk, and K.M. Young for their support of this work, which was performed under DOE contract # DE-AC02-76-CH03073.

Table 1 - Examples of MHD-Induced Alpha Loss in TFTR

Shot	I (MA)	B(T)	R(m)	P*(MW)	MHD Type	Time (s)
74808	1.0	4.8	2.45	3.7	major dis.	3.327±0.0005
76773	2.5	5.1	2.52	7.9	minor dis.	3.922±0.0002
76778	2.5	5.1	2.52	9.3	major dis.	3.952±0.001
77309	2.1	5.1	2.52	5.4	KBM	4.4±0.02
77801	1.0	4.8	2.45	1.4	sawtooth	3.024±0.0005
78607	1.0	4.9	2.45	1.7	fishbone	3.181±0.001
78608	1.0	4.9	2.45	1.1	sawtooth	2.836±0.0001
	1.0	4.9	2.45	0.3	major dis.	3.302±0.0001
79175	1.4	4.9	2.52	1.8	sawtooth	4.100±0.0004
79369	1.6	4.8	2.52	1.3	2/1+3/2	4.0-4.5
	1.6	4.8	2.52	1.7	minor dis.	3.872±0.0001
79983	1.6	4.8	2.52	3.1	minor dis.	3.997±0.001
80539	2.7	5.5	2.52	10.7	minor dis.	3.785±0.0002
83546	2.3	5.5	2.52	2.8	major dis.	4.735±0.002
84529	2.0	5.1	2.52	3.9	sawtooth	3.372±0.0005
86009	1.0	4.8	2.52	2.3	minor dis.	3.673±0.0002
86289	1.5	4.9	2.45	2.5	2/1+1/1	3.4-3.6
87530	1.4	3.4	2.52	0.4	sawtooth	4.61±0.0001
89725	2.3	5.8	2.52	6.5	KBM	4.4-4.5
92397	2.3	5.1	2.52	2.5	2/1	3.5-3.6
104250	1.8	5.5	2.52	0.8	3/1	2.4-2.8

* Fusion power at time of MHD activity

Figures

1) Example of coherent MHD-induced alpha loss in a standard TFTR DT supershot with $I=1.5$ MA and 15 MW of NBI. This discharge had $m/n=2/1+1/1$ modes at about 1 kHz, which caused an increase in alpha loss by up to $\approx 25\%$ in the midplane detector. The midplane detector aperture in this discharge was at -2 cm with respect to the limiter shadow.

2) Example of alpha loss caused by fishbone bursts. This discharge was a low current DT supershot which had a current ramp-down prior to NBI in order to induce H-modes. Each fishbone burst caused an increase in the alpha loss in the 90° detector of 10-100%, when compared with the MHD-quiescent first-orbit alpha loss level between bursts. The MHD mode frequency decreased significantly during each burst, and the dominant mode number was $m/n=1/1$.

3) Example of MHD-induced alpha loss during a high-powered DT supershot with $I=2.3$ MA and 27 MW of NBI. The alpha loss increased by up to a factor of ≈ 2 in the 60° detector, with less of an increase in the 90° detector and very little increase in the 45° detector (the 20° detector was not inserted). The dominant MHD mode was $m/n=2/1$ at ≈ 300 Hz in this case.

4) Example of the effect of a large very low frequency $m/n=3/1$ MHD mode on alpha loss in a discharge with weak magnetic shear (#104250). In this case the MHD mode apparently caused a significant degradation of the plasma confinement, in contrast with the very similar discharge shown without MHD (#104253). The alpha loss in the 20° detector was strongly modulated at the MHD frequency but did not increase with respect to a very similar shot without MHD. The 20° detector was at -3 cm with respect to the outer limiter in both cases.

5) Example of MHD-induced alpha loss in a $I=1.6$ MA discharge which had a minor disruption at 3.8 sec (possibly caused by a flake from the wall), followed by a large coherent $m/n=2/1$ and $3/2$ mode. The alpha loss was modulated most strongly in the 45° detector, with relatively little effect in the 90° or 60° detectors.

6) Example of the effect of a major disruption on alpha loss. This $I=2.3$ MA, 15 MW NBI discharge had a beta limiting disruption which caused the alpha loss to transiently increase by a factor of up to ≈ 200 in the 90° detector during the thermal quench just before the plasma current decay. The duration of this very large burst of alpha loss was only about 1 msec.

7) Example of the effect of a minor disruption on alpha loss in a discharge near the beta limit at $I=2.5$ MA and 30 MW of NBI. The minor disruption caused a $\approx 20\%$ drop in the neutron rate within ≈ 0.1 msec, during which time the alpha loss increased by a factor of ≈ 6 in the 90° detector. The 60° detector showed a very brief burst of loss, while the 45° detector showed no perceptible loss. The 20° detector was not inserted during this discharge.

8) Examples of the effect of sawtooth crashes on alpha loss during a low $q(a)$ discharge with low toroidal field ($B=3.4$ T) and low NBI heating power (8 MW). The top panel shows that these sawteeth, which were preceded by growing $m/n=1/1$ modes, each increased the alpha loss rate in the 20° detectors by about a factor of 2. The fast time evolution during a ≈ 0.1 msec period was different for each alpha loss detector, as shown at the bottom for a very similar discharge, for which the midplane detector was at -0.5 cm.

9) Example of the effect of a sawtooth crash on alpha loss during a moderate-powered ST supershot with $I=1.4$ MA and 15 MN NBI. In this case the single sawtooth crash caused a factor of 5 increase in the alpha loss at 90° , and less of an increase in the 60° and 45° detectors.

10) Pitch angle and gyroradius distributions of the alpha loss in the 20° detector for the example in Fig. 1. There is no significant difference in these distributions between time periods before (3.25-3.35 sec), during (3.5-3.55 sec), or after (3.6-3.65 sec) the MHD-induced alpha loss. These curves are normalized to each other at their peaks to show more clearly the shapes of the distributions.

11) Pitch angle vs. gyroradius patterns seen in the 20° detector during the very slow coherent MHD activity of Fig. 4. There is a significant difference between the pitch angle distributions at the times of maximum (a) and minimum (b) and (c) alpha loss signals. The pattern in a similar discharge without MHD activity in (d) is approximately the same as the time-average of the pattern seen at the maximum MHD activity in (a).

12) Pitch angle vs. gyroradius distributions in the 90° and 20° detectors during a major disruption. There is a significant component of partially thermalized alpha loss seen during the disruption in the 90° detector, and to a lesser extent in the 20° detector. This discharge had parameters similar to that shown in Fig. 2.

13) Pitch angle and gyroradius distributions seen in the 90° detector during a sawtooth crash in the discharge of Fig. 9. The sawtooth-induced alpha loss occurred near the passing-trapped boundary at 60° pitch angle, but with a gyroradius distribution not significantly different from that seen before or after the sawtooth crash.

14) Peak MHD-induced alpha loss rate as measured in the 90° detector for various types of MHD activity. Each point represents one case listed in Table 1, and all data is normalized to the DT neutron rate at the time of the MHD. The MHD-quiescent first-orbit alpha loss has been subtracted out from the data, but is shown separately by the shaded region (its range is due

to the varying plasma currents). For example, the instantaneous alpha loss during disruptions can be up to ≈ 1000 times the first-orbit loss.

15) Relationship between the measured alpha loss rate due to MHD activity in the 90° detector (vertical) and the percentage drop in the DT neutron rate during this MHD activity (horizontal). This percentage neutron drop is a rough measurement of the degree to which this MHD activity perturbs the core of the plasma. The data shown at a “1%” drop indicate no measurable change in neutron rate, while the data shown at a “100%” drop indicate a major disruption during which the neutron rate drops to zero.

16) Example of the fluctuations in the electron temperature profile during coherent MHD activity in TFTR, obtained from the ECE radiometer array. This case shows an ≈ 4 cm local radial displacement caused by an MHD mode between $R= 270 - 320$ cm, associated with the moderately large $m/n=2/1 + 1/1$ mode activity and alpha loss shown in Fig. 3 (shot #92397).

17) Relationship between the measured alpha loss rate due to MHD in the 90° detector and the estimated size of the radial displacement due to the MHD, as measured by the ECE emission profile. Each “x” corresponds to one shot at the time indicated in Table 1. The range of displacements in this data set was $\approx 1-10$ cm, but there was not a clear correlation between these widths and the amount of MHD-induced alpha loss. The smallest perturbed regions were associated with high frequency kinetic ballooning mode (KBM) activity, but no disruptions were included in this plot, since their perturbations widths could not be uniquely defined.

18) Poloidal distributions of MHD-induced alpha loss for the same set of data shown in Fig. 14. The poloidal distributions are generally peaked toward the vessel bottom for reconnection events (disruptions and sawteeth), are broader and more variable for the coherent MHD. The vertical scales are the same as for Fig. 14. The first-orbit loss level is

approximately between 0.1 and 1 for this range of poloidal angles (depending on the plasma current).

19) Ratio of the MHD-induced alpha loss measured in the 20° detector to that observed at the same time in the 90° detector. This ratio generally increases as the 20° detector aperture is moved inward toward the plasma (to the left in this figure), but there is considerable scatter at a fixed radial position depending on the type of MHD. The geometrical shadow of the outer poloidal ring limiters is shown by the shaded region at the bottom.

20) Estimate of the MHD-induced alpha loss fraction for various types of MHD activity in TFTR, averaged over the three fixed poloidal detectors and the duration of the MHD activity. The vertical scales are rough order-of-magnitude estimates for the alpha loss fractions; for example, the alpha loss during a single sawtooth event is <0.01%, i.e. negligible with respect to that during a major disruption. The major uncertainty is the lack of spatial information on alpha loss at locations other than at the 3 fixed detectors.

21) Example of a relatively small effect of coherent MHD on alpha loss in the 90° detector during a discharge with a weak neutron “rollover”. This case had a 3/2 mode at 16 kHz, and caused no measurable modulation in the alpha loss, but did correlate with a slow $\approx 25\%$ increase in the neutron-normalized alpha loss as this mode grew in time. The neutron-normalized alpha loss was smoothed over 1 msec to reduce the noise level.

22) Example of a sawtooth crash in which there was no visible burst in the 20° detector, even though there was a sawtooth-induced burst of alpha loss in the 90° detector. The 20° detector position was -2 cm in this case, and the sawtooth occurred just after the end of NBI. The neutron background was not subtracted from the 90° signal in this case.

23) Illustration of a single guiding center alpha particle orbit in the presence of a $\Delta=20$ cm wide $m/n=2/1$ MHD island in an $I=1.4$ MA TFTR discharge. This orbit is launched in a co-going direction at $R=307$ cm, and diffuses to the wall after ≈ 100 toroidal transits. The outer midplane crossing position as shown at the bottom varies by an average of 8 cm per transit. The purely oscillatory motion of a zero-energy ion following the field line in the island is also shown at the bottom. There are no collisions or TF ripple present in this simulation.

24) Map of the alpha loss regions in birth position vs. pitch angle for the example of Fig. 23. The horizontal axis is the birth location of alphas along the outer midplane, while the vertical axis is their pitch at birth, in units of \cos (pitch). Most of the MHD-induced alpha loss occurs for co-passing alphas born at large major radii, but some alpha loss occurs for initially counter-passing alphas which are born nearer the center and move across the passing-trapped boundary.

25) Poloidal and toroidal distributions from a Monte Carlo simulation of the MHD-induced alpha loss for the Fig. 24. The poloidal distributions are peaked within $\approx 60^\circ$ below the outer and inner midplane, corresponding to the loss of co- and counter-going alphas, respectively. There is relatively little alpha loss predicted near the vessel bottom for this case.

26) Modeling of the total alpha loss for the $I=1.4$ MA case versus mode number and magnetic island width. Each point represents a guiding center code run with 500-5000 alpha particles for 1000 toroidal transits. The range of the experimental data set for coherent modes is shown by the shaded region. This data set contains plasma currents in the range $I=1.0$ - 2.3 MA, so does not exactly correspond to these calculations at $I=1.4$ MA.

27) Comparison of the measured and modeled alpha loss for the specific coherent mode corresponding to Fig. 3. The modeling as shown by the “x”

points is done for 2/1 modes in an $I=2.3$ MA, $R=2.52$ m plasma, with one case (at 4 cm island width) run with an additional 1/1 mode present to better model the observed perturbation near $q=1$ shown in Fig. 16. The range of data for the time-averaged alpha loss in the three fixed detectors is shown by the shaded region located at the measured island width of 4 ± 1 cm.

28) Illustration of the qualitative effect of reconnection on alpha loss across the passing-trapped boundary. The top part shows an initially counter-passing orbit near the plasma center which is lost across the passing-trapped boundary due to MHD-induced transport from a 2/1 mode. The bottom part shows the location of this loss orbit (A) in the map of initial alpha birth radius versus pitch angle. Alphas in the shaded region to the left of A can be lost at A due to reconnection-induced transport. Alphas lost at B and C hit the wall near the outer and inner midplanes, respectively.

29) Variation of the calculated MHD-induced alpha loss for a $\Delta=20$ cm wide $m/n=2/1$ island versus the effective alpha confinement parameter ρ_α/a . In all cases the Monte Carlo simulations were the same type as for the $I=1.4$ MA case of Figs. 25 (e.g. with 1000 toroidal transits), but with a ρ_α/a varied by changing the assumed birth energy. At the top are the poloidal distributions of MHD-induced alpha loss for higher plasma currents than for Fig. 25. The bottom part shows the calculated global MHD-induced alpha loss versus ρ_α/a for a TFTR-like plasma geometry.

References

- [1] E.D. Fredrickson et al, Proc. Proc. 15th Conf. on Fusion Energy, Seville (1994), IAEA, Vienna (1995) p. 275
- [2] S.J. Zweben et al, Phys. Plasmas **1** (5) 1469 (1993)
- [3] R. Nazikian et al, Phys. Rev. Lett. **78**, 2976 (1997)
- [4] W.W. Heidbrink and G. Sadler, Nucl. Fusion **34**, 535 (1994)
- [5] W.W. Heidbrink et al, Nucl. Fus. **23**, 917 (1983)
- [6] H. Duong and W.W. Heidbrink, Nucl. Fusion **33**, 211 (1993)
- [7] E. Bittoni and M. Haegi, Fusion Tech. **22**, 461 (1992)
- [8] D.J. Sigmar et al, Phys. Fluids **B4**, 1506 (1992)
- [9] R.B. White and H.E. Mynick, Phys. Fluids **B1**, 980 (1989)
- [10] S. Konovolov and S.V. Putvinskii, Fusion Technol. **18**, 397 (1990)
- [11] H.E. Mynick, Phys. Fluids **B5**, 3490 (1993); also, H.E. Mynick, Phys. Fluids **B5**, 1471 (1993)
- [12] Ya. Kolesnichenko et al, Phys. Plasmas **5**, 2963 (1998); also, Ya. Kolesnichenko et al, Phys. Plasmas **5**, 729 (1998)
- [13] Ya. Kolesnichenko et al, Proc. 17th Fusion Energy Conf, Yokohama (1998)
- [14] N.N. Gorelenkov et al, Nucl. Fus. **37**, 1053 (1997)
- [15] D.S. Darrow et al, Rev. Sci. Inst. **66**, 476 (1995)
- [16] S.J. Zweben et al, Nucl. Fusion **35**, 893 (1995)
- [17] S.J. Zweben et al, Nucl. Fus. **38**, 739 (1998)
- [18] Z. Chang et al, Phys. Plasmas **5**, 1076 (1998)
- [19] S. Mirnov et al, Phys. Plasmas **5**, 3950 (1998)
- [20] S. von Goeler et al, Rev. Sci. Inst. **57**, 473 (1996)
- [21] F. B. Marcus et al, Plasma Phys. and Cont. Fusion **33**, 277 (1991)
- [22] W.W. Heidbrink et al, Phys. Rev. Lett. **53**, 1905 (1984)

- [23] Z. Chang et al, Phys. Rev. Lett. **76**, 1071 (1996)
- [24] C.E. Bush et al, Phys. Plasmas **2**, 2366 (1995)
- [25] S.S. Medley et al, Nucl. Fus. **38**, 1283 (1998)
- [26] B.C. Stratton et al, Nucl. Fus. **36**, 1586 (1996)
- [27] E.D. Fredrickson et al, Phys. Plasmas **4**, 1589 (1997)
- [28] D.K. Mansfield et al, Phys. Plasmas **3**, 1892 (1996)
- [29] J. D. Strachan et al, "TFTR Rollover" submitted to Nucl. Fusion (1998)
- [30] H. Takahashi, Fusion Eng. and Design **34**, 89 (1997)
- [31] C.B. Forest et al, Phys. Rev. Lett. **79**, 427 (1997)
- [32] R.B. White and M.S. Chance, Phys. Fluids **27**, 2455 (1984)
- [33] B.C. Stratton et al, to be published in Nucl. Fus. 1999
- [34] S.J. Zweben et al, Nucl. Fus. **31**, 2219 (1991)
- [35] W. Park et al, Phys. Rev. Lett. **75**, 1763 (1995)
- [36] S.V. Putvinskii et al, Nucl. Fus. **38**, 1275 (1998)

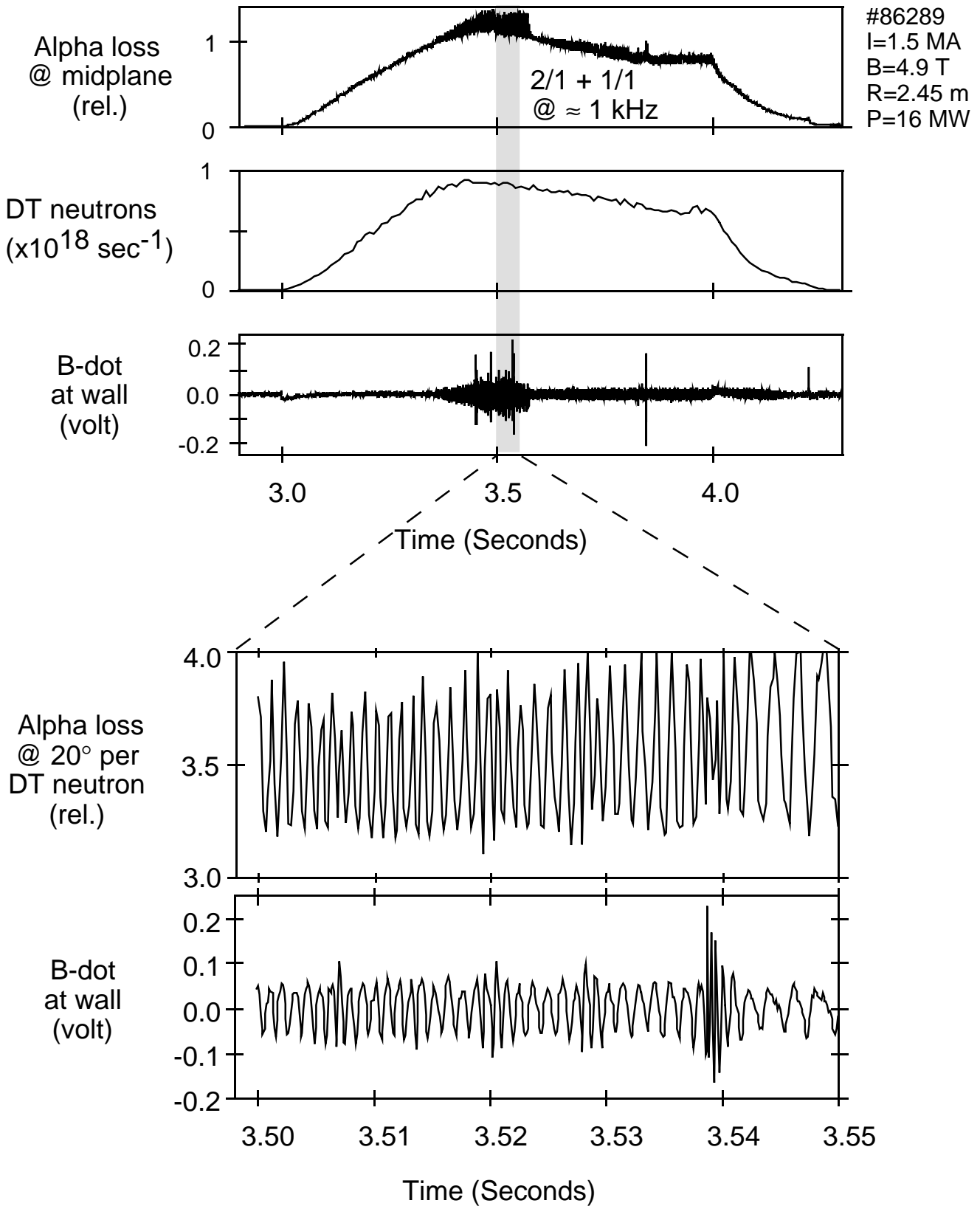


Fig. 1

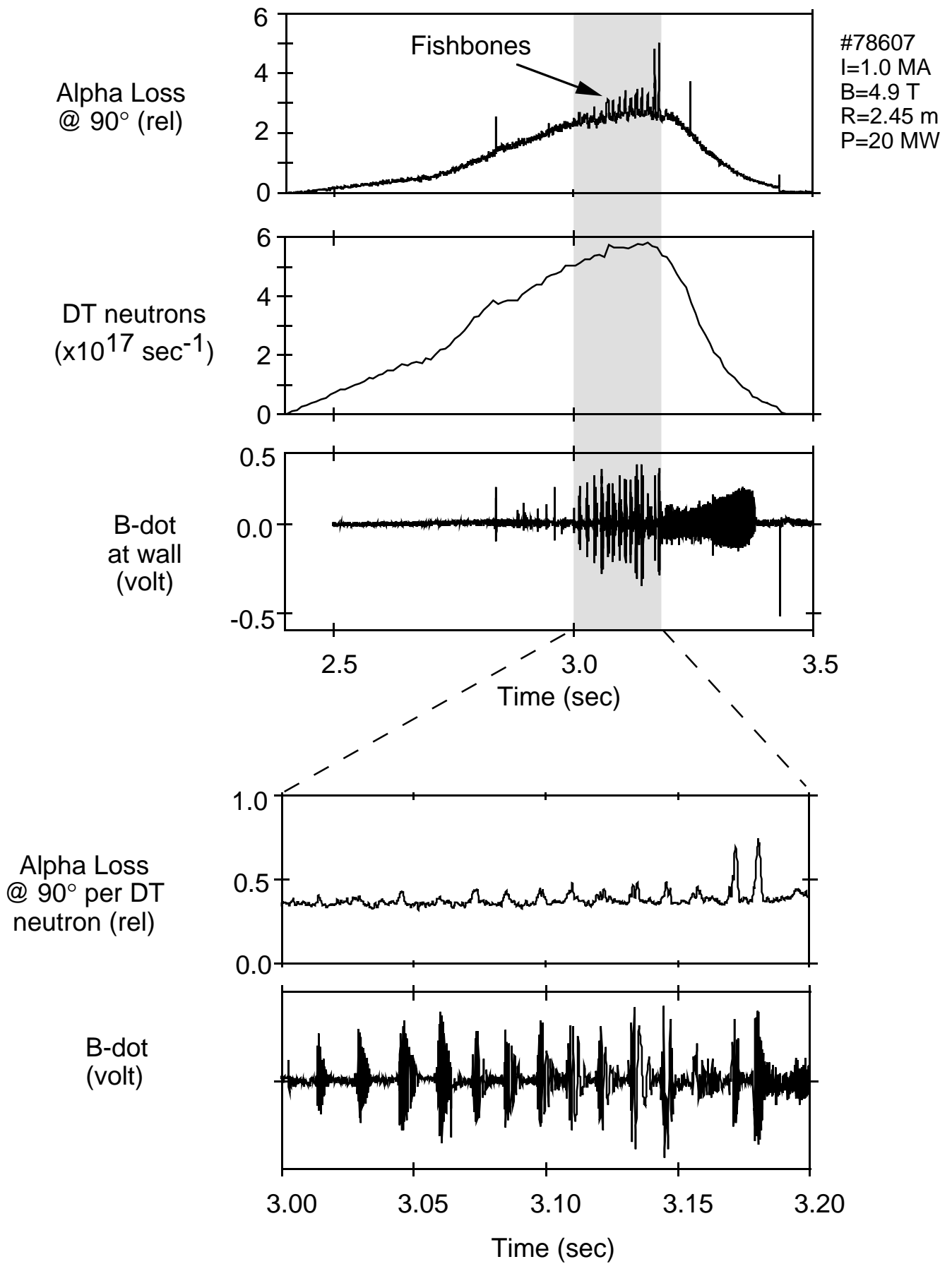


Fig. 2

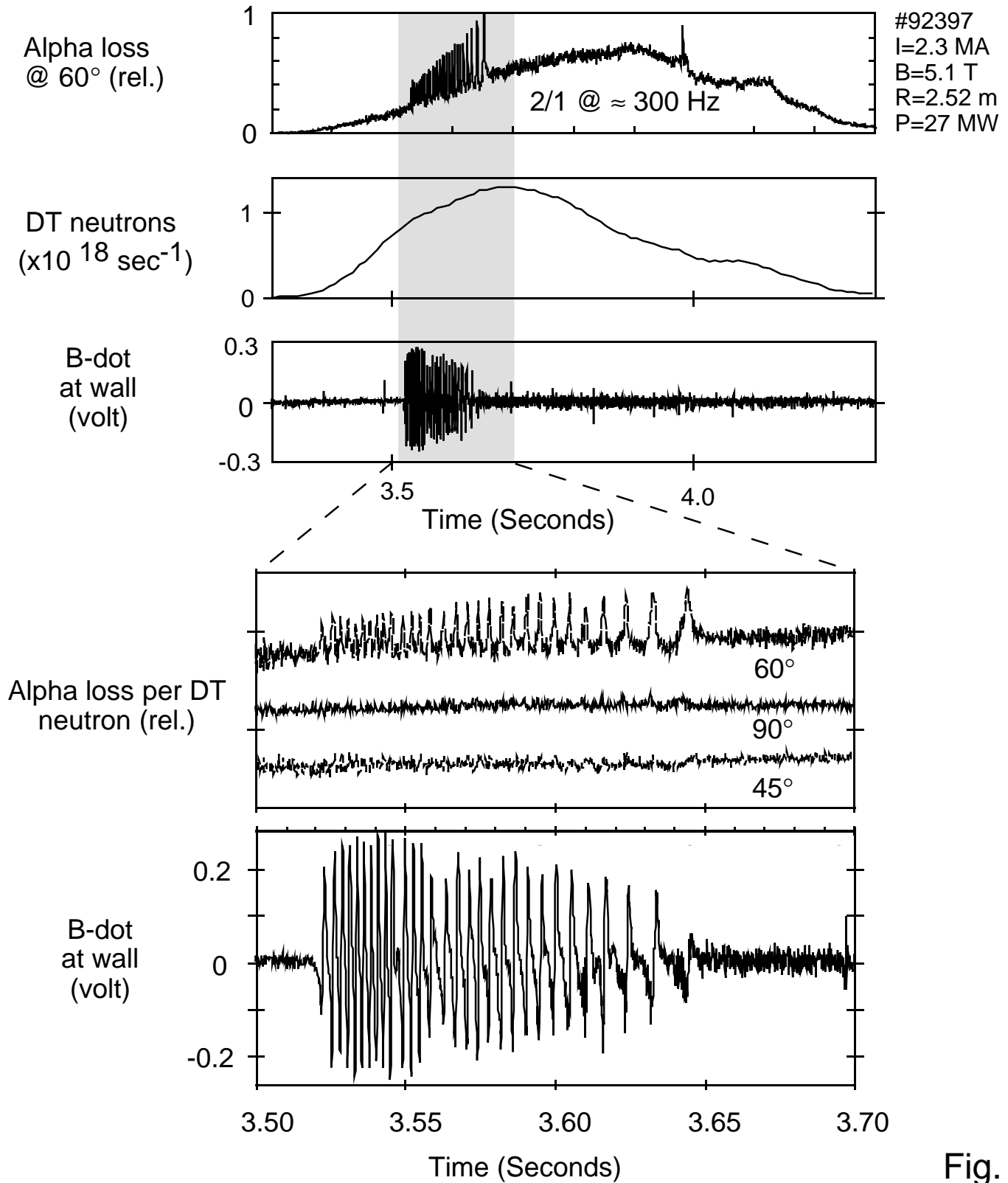


Fig. 3

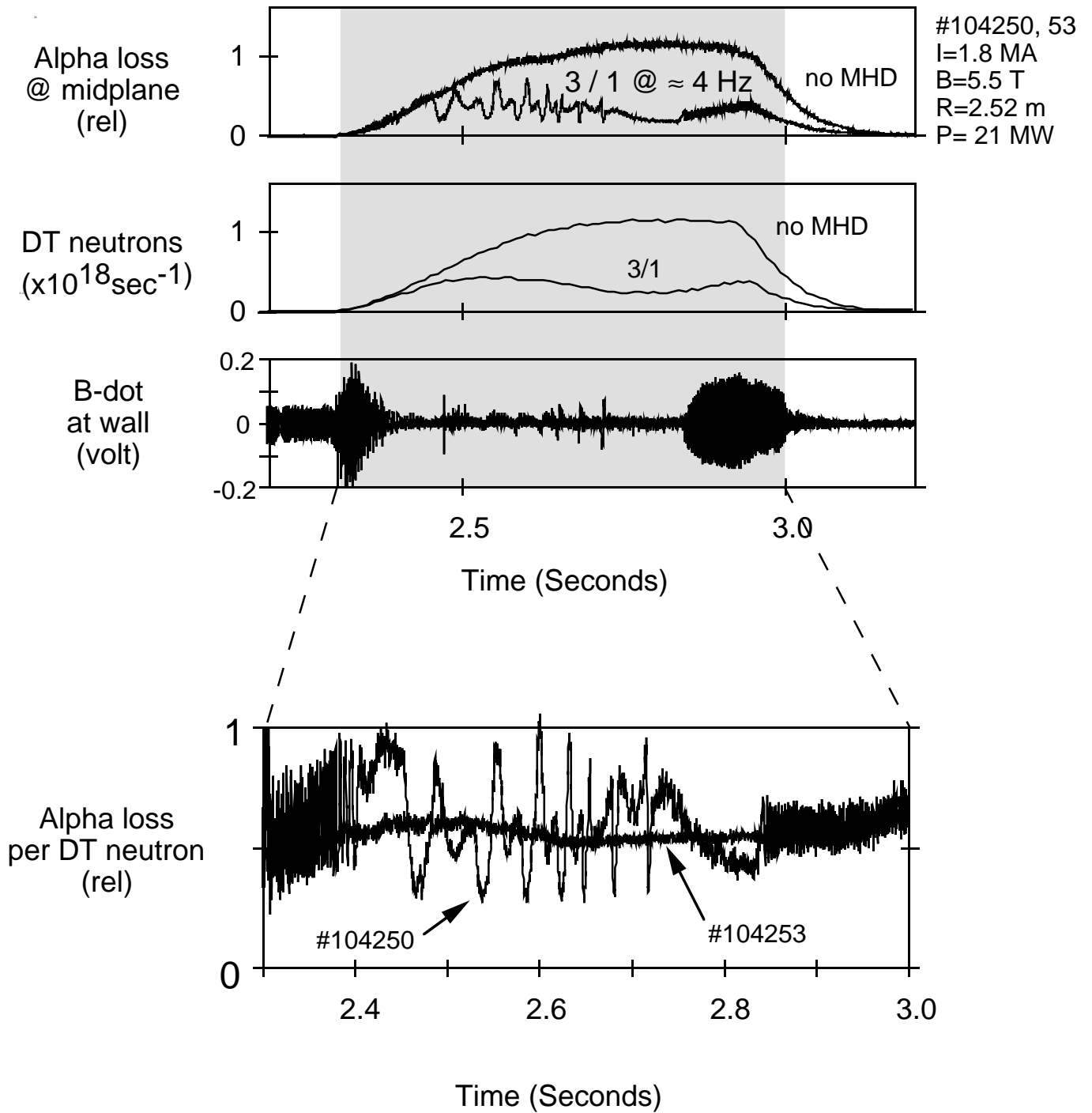


Fig. 4

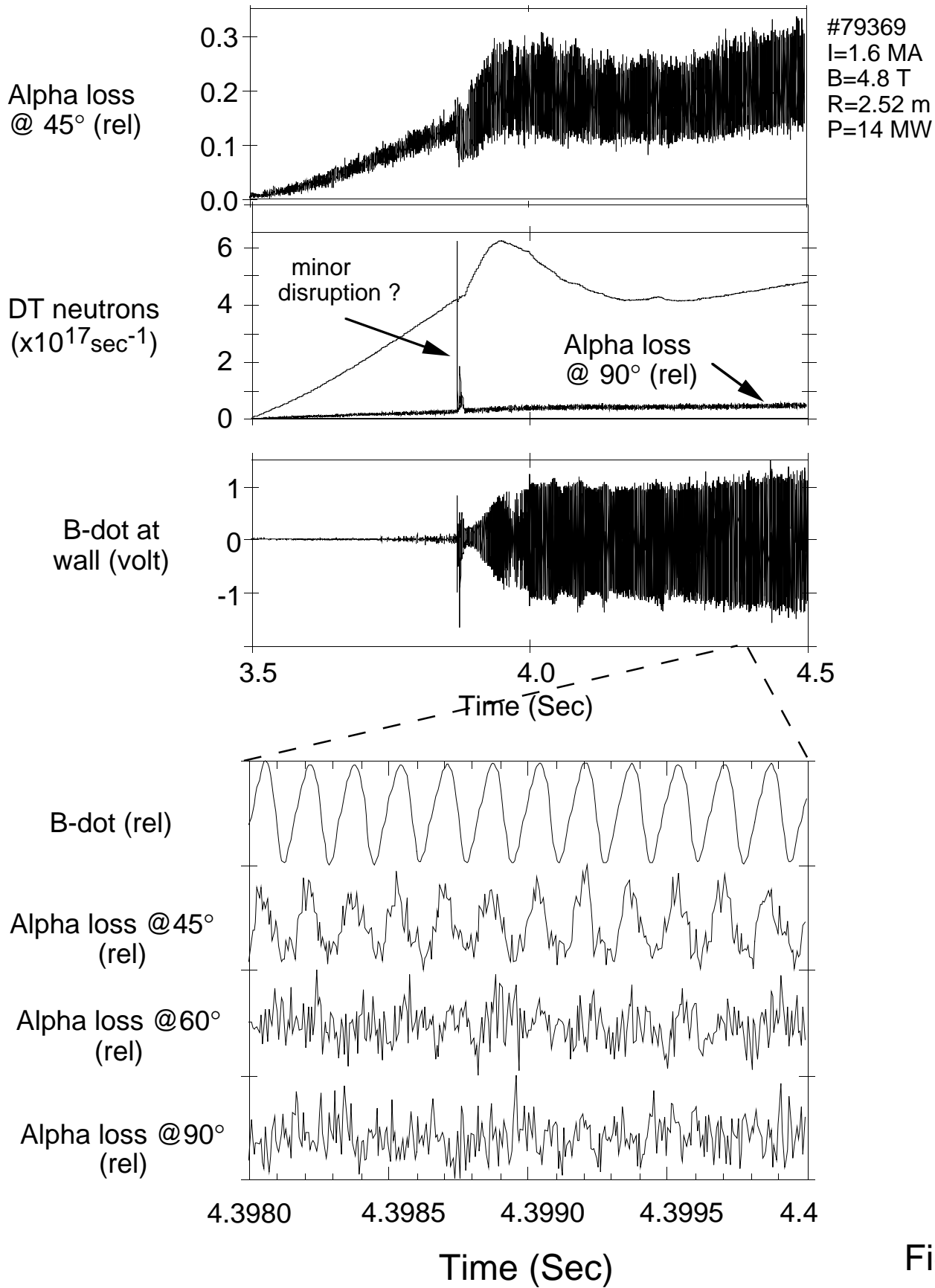


Fig. 5

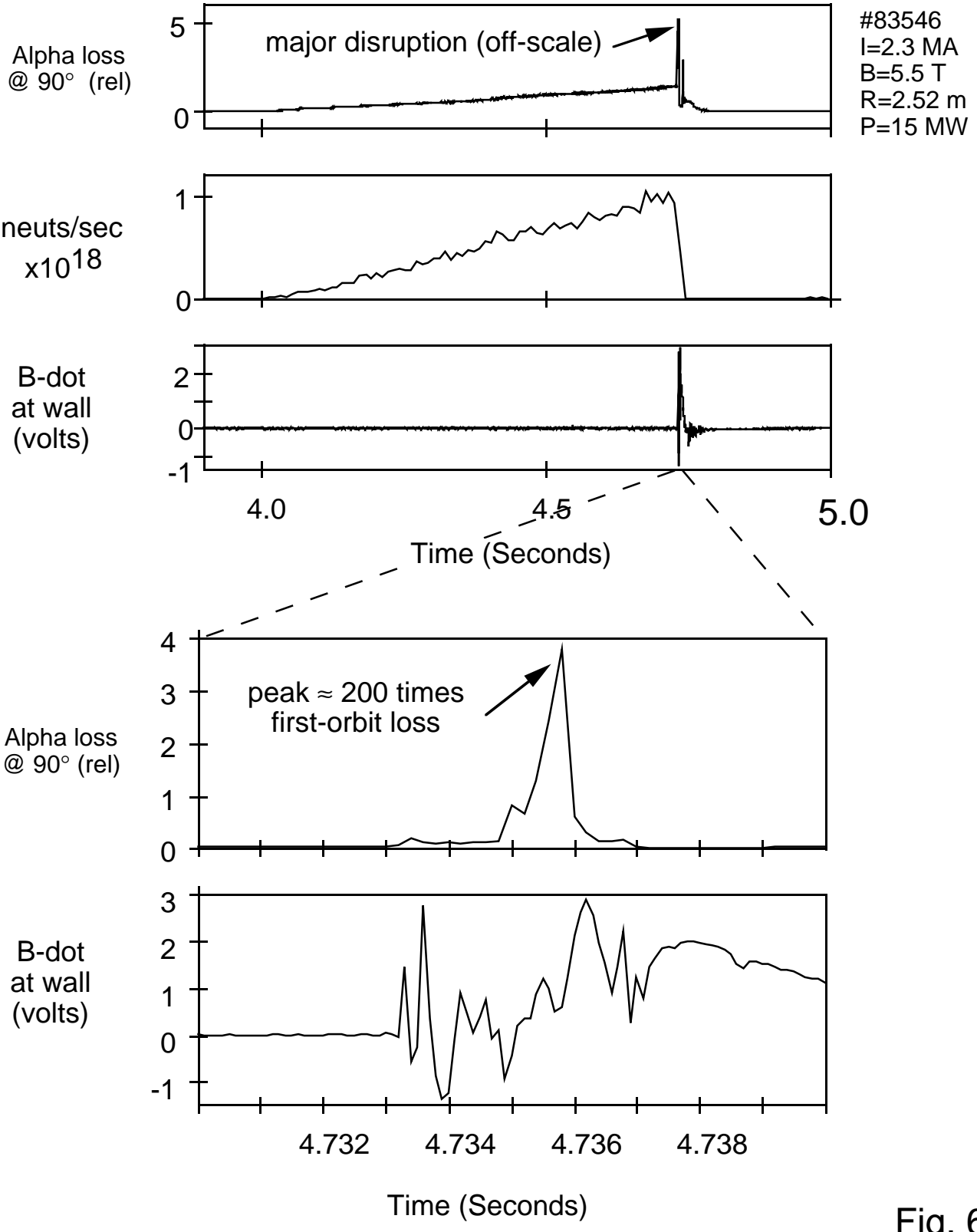
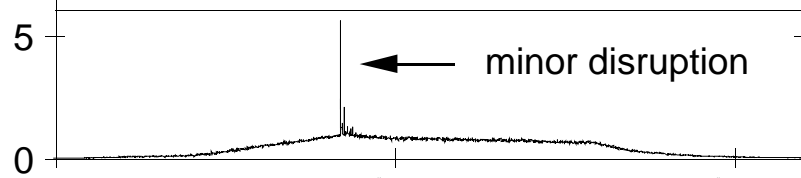


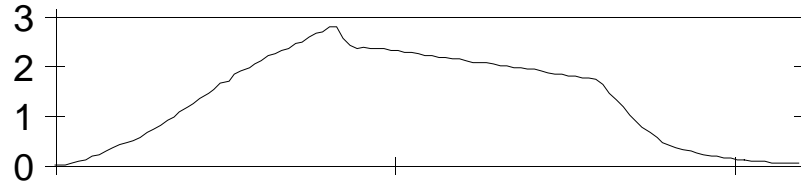
Fig. 6

Alpha loss
@ 90° (rel)

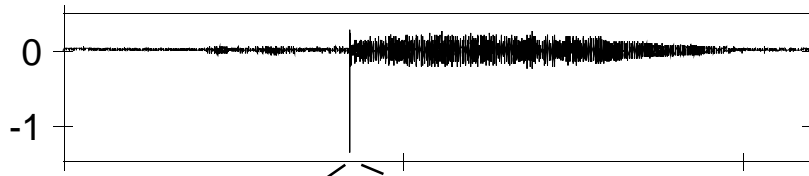


#76773
I=2.5 MA
B=5.1 T
R=2.52 m
P=30 MW

DT neutrons
($\times 10^{18} \text{ sec}^{-1}$)

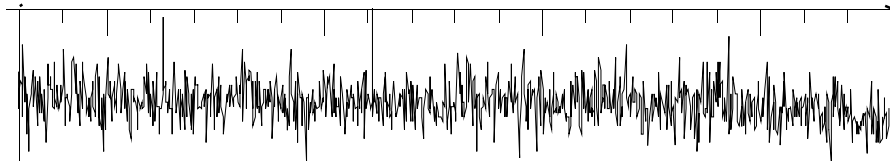


B-dot at
wall (rel)

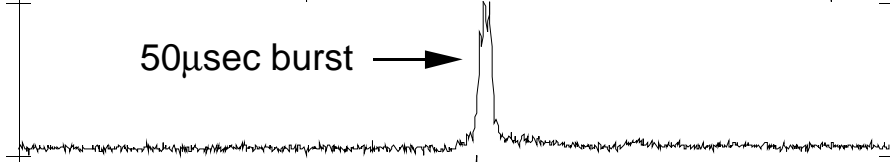


3.5 4.0 4.5
Time (sec.)

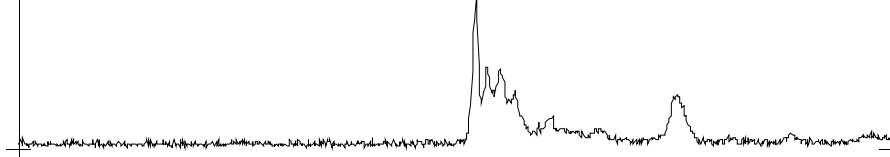
Alpha loss
@ 45° (rel)



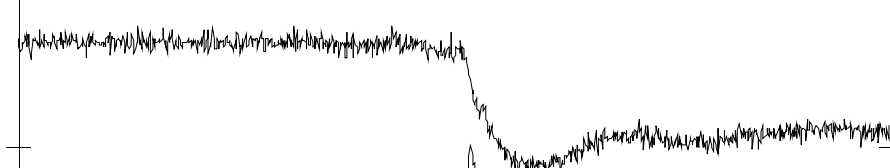
Alpha loss
@ 60° (rel)



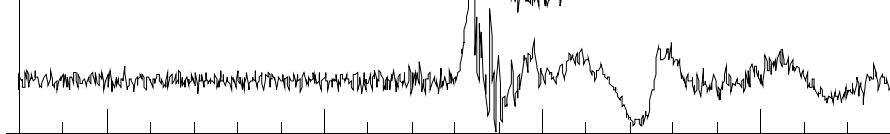
Alpha loss
@ 90° (rel)



DT neutrons
(rel)



B-dot @
wall (rel)



3.9215 3.9220 3.9225 3.9230

Time (sec)

Fig. 7

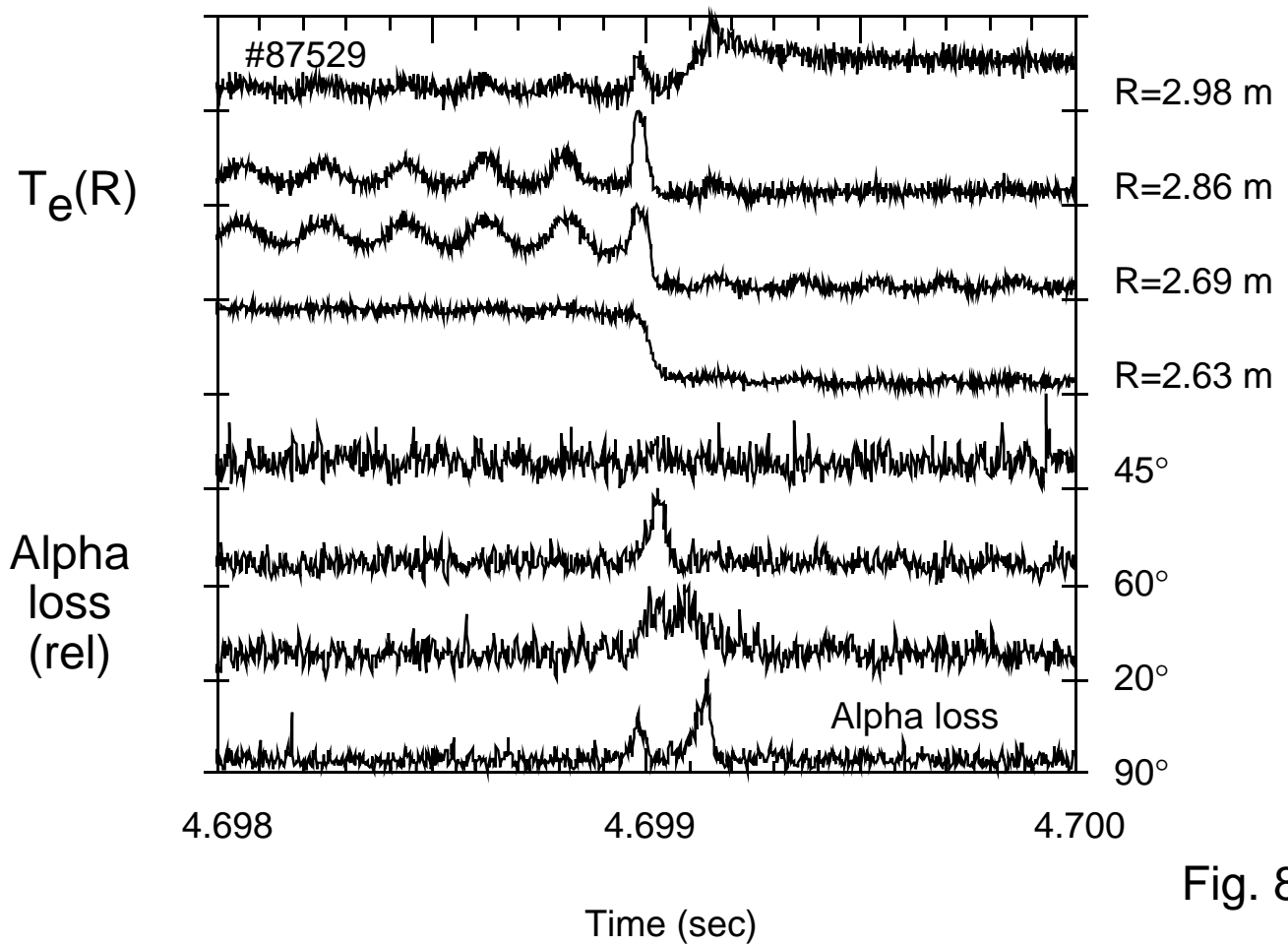
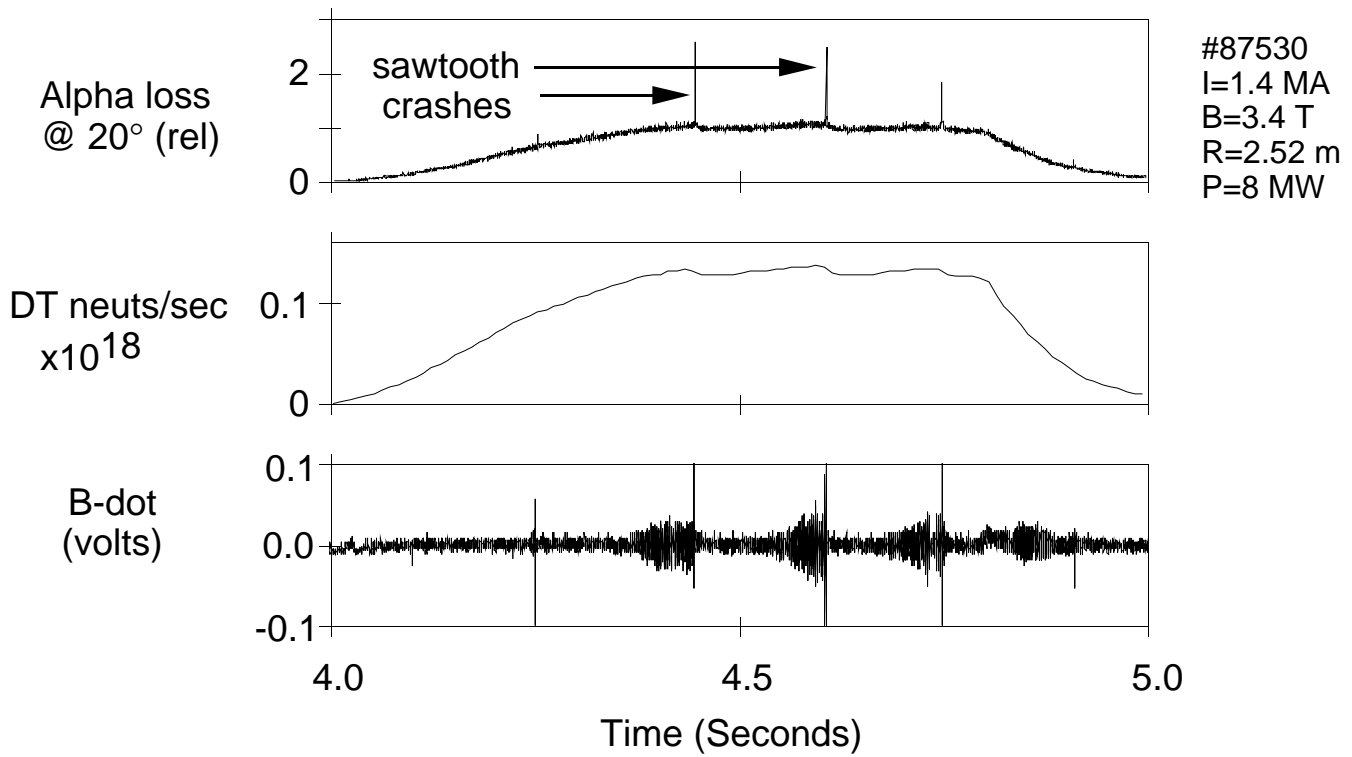


Fig. 8

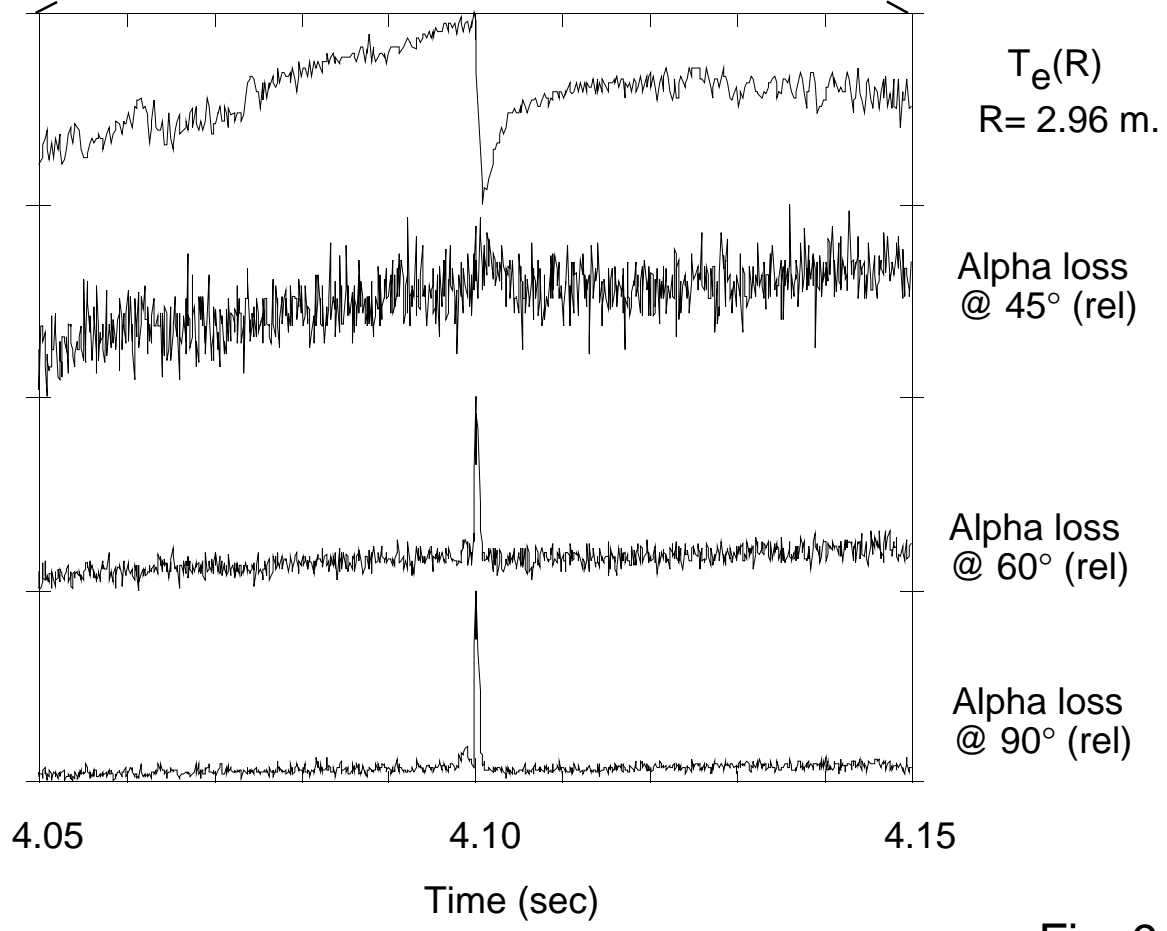
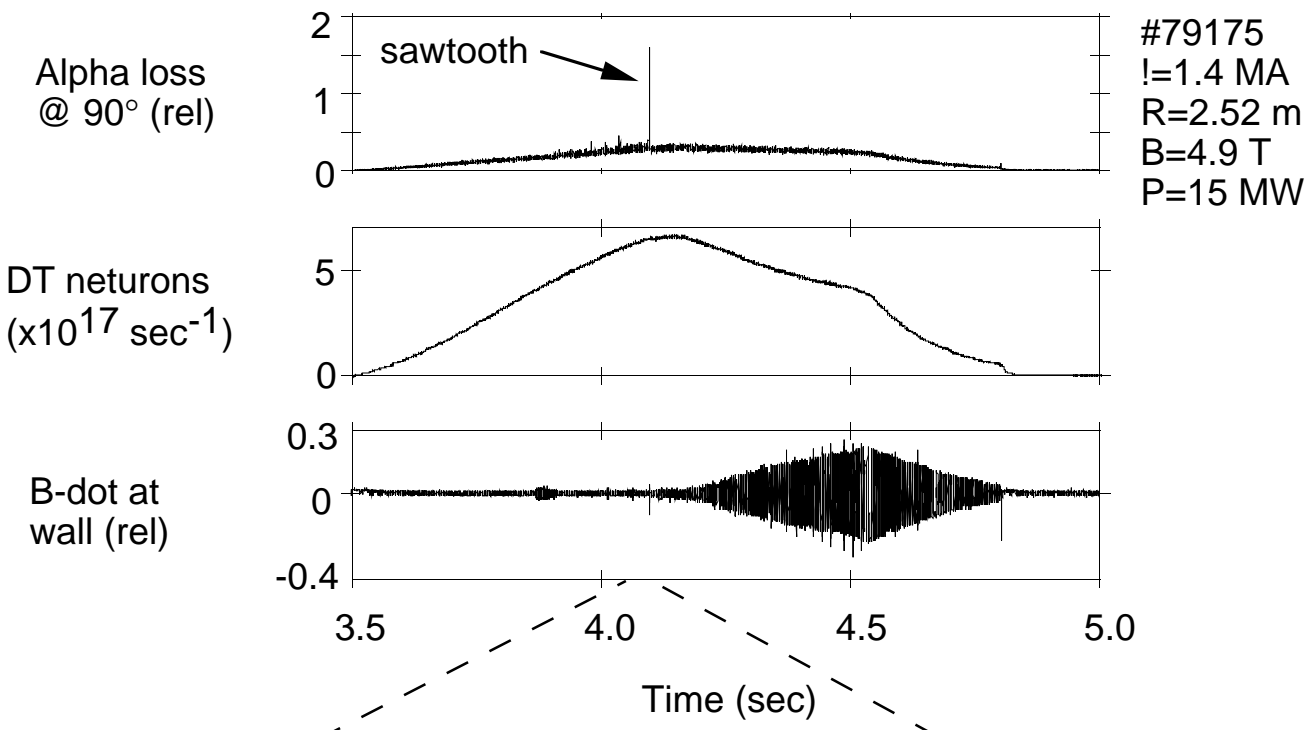


Fig. 9

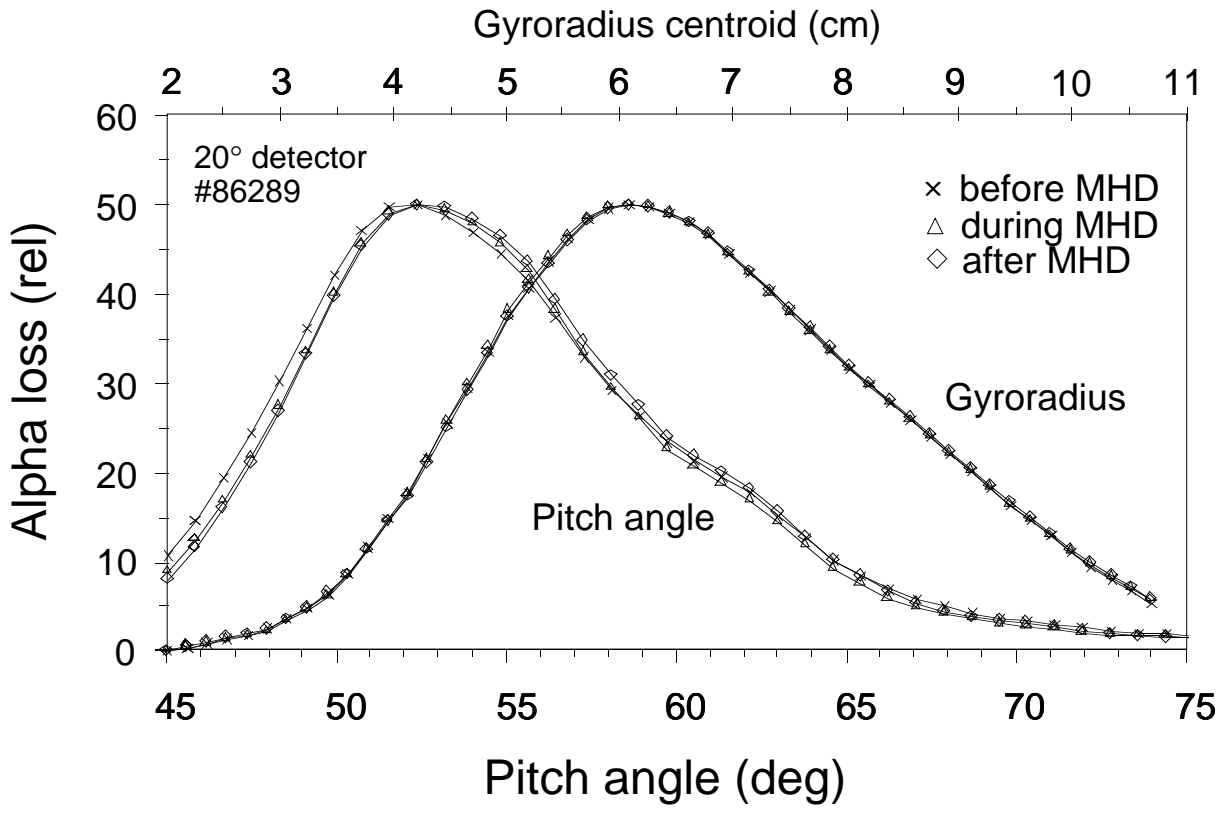


Fig. 10

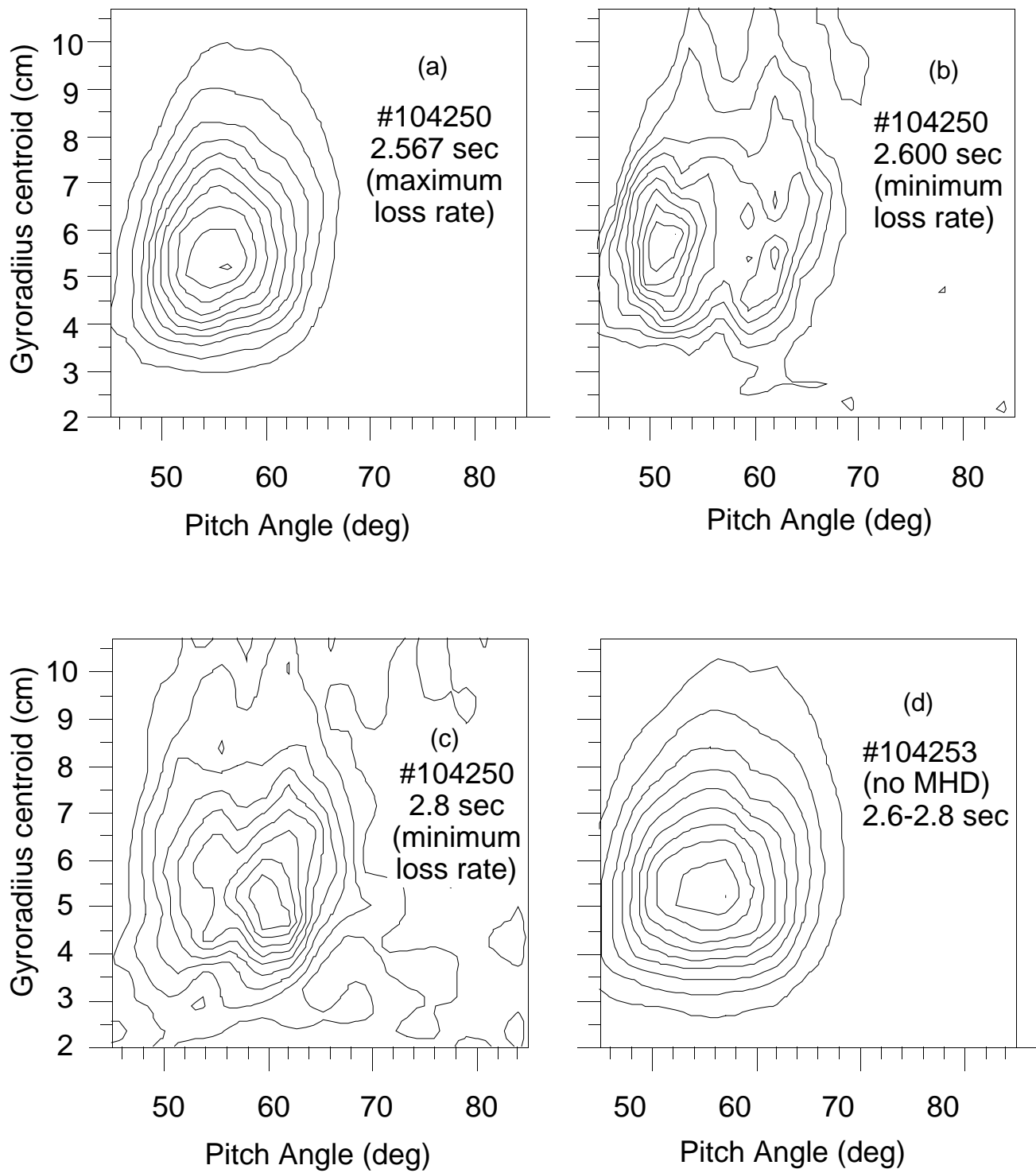


Fig. 11

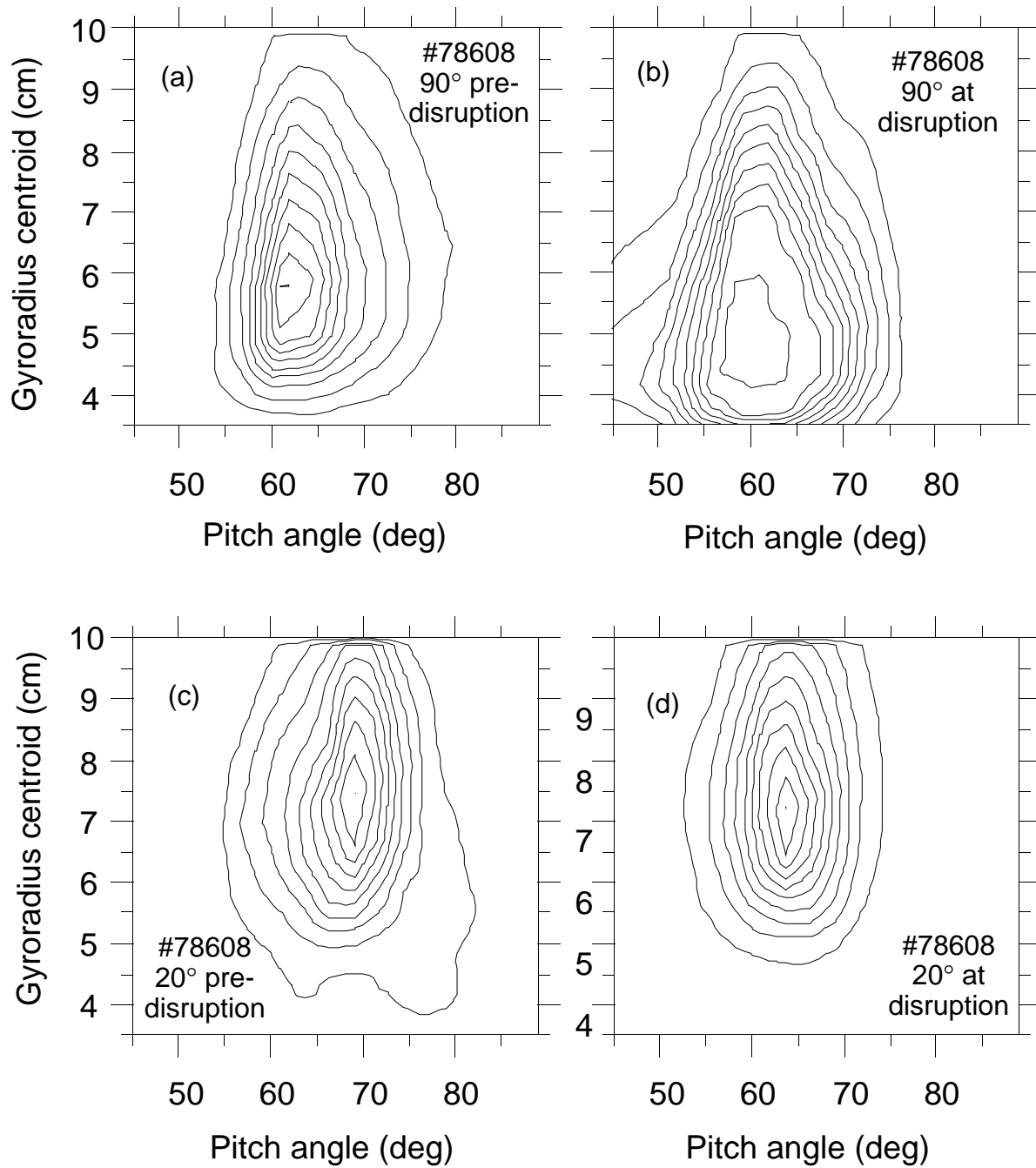


Fig. 12

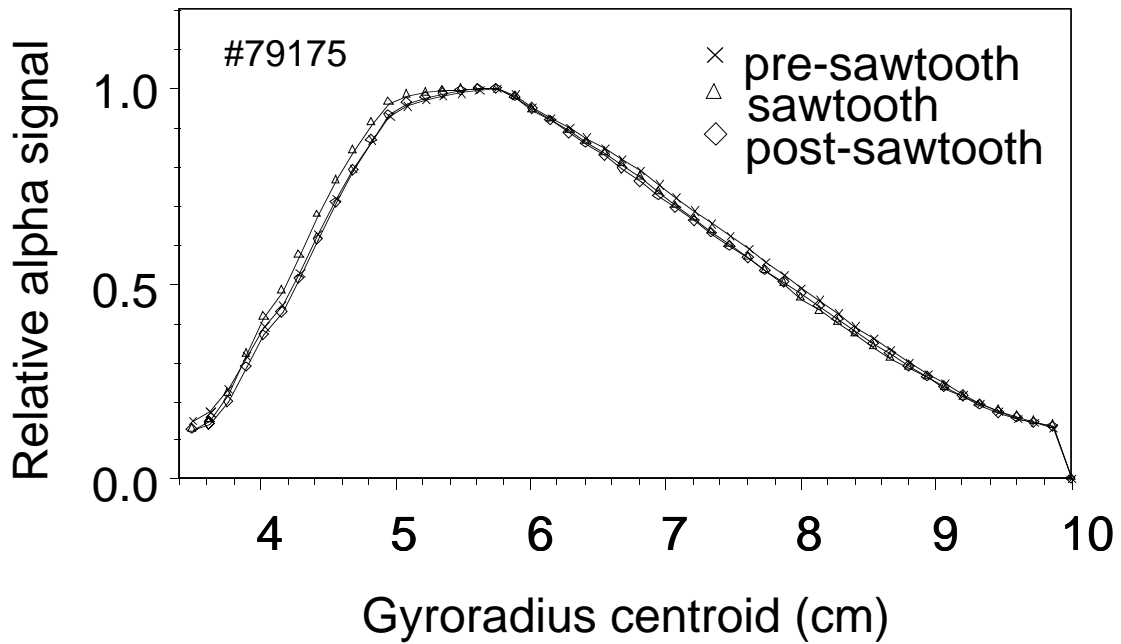
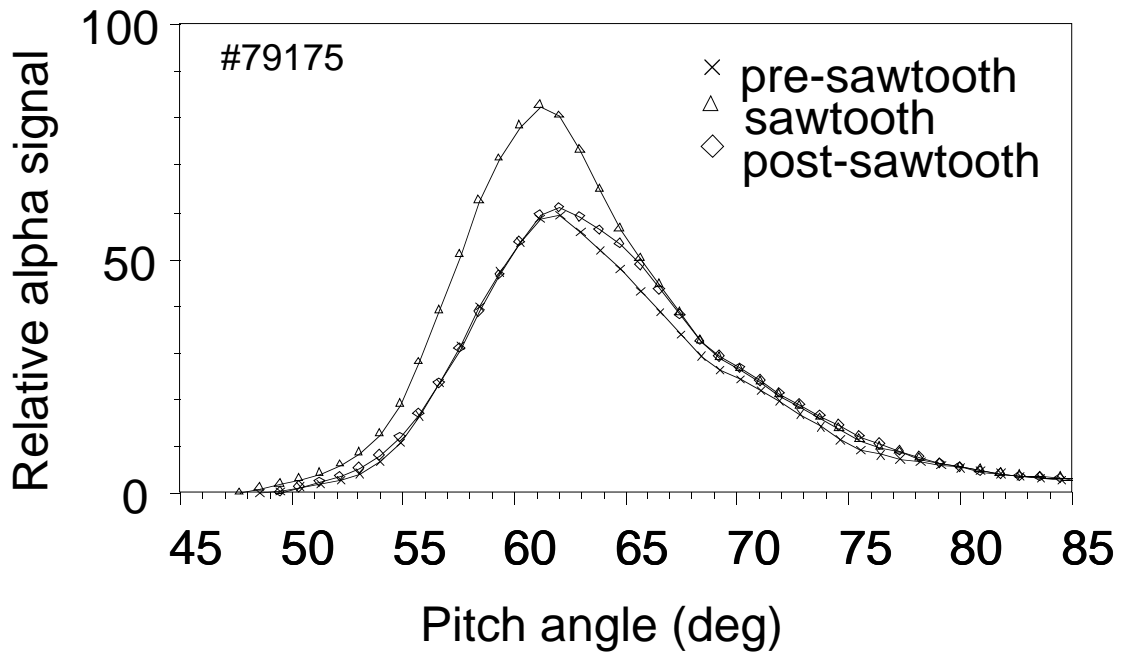


Fig. 13

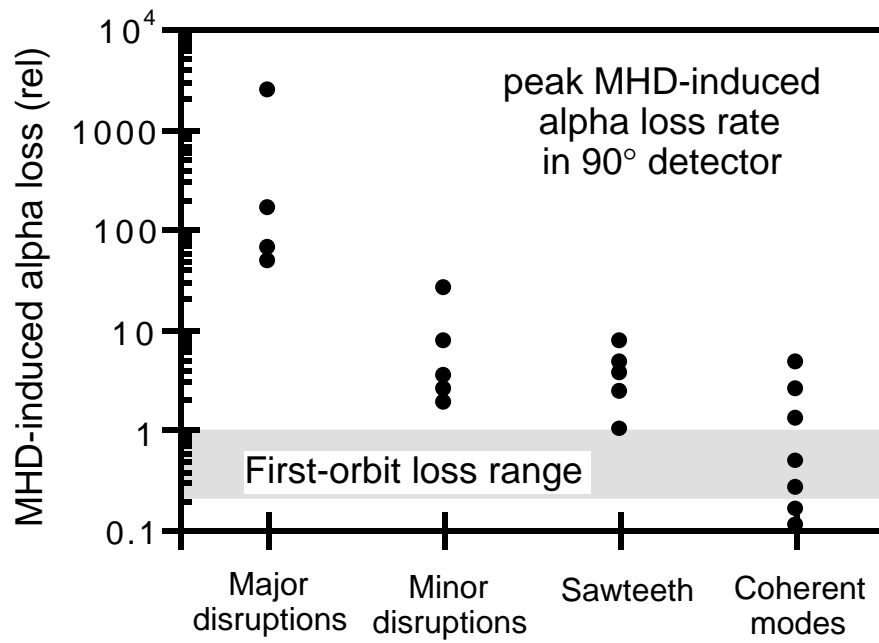


Fig. 14

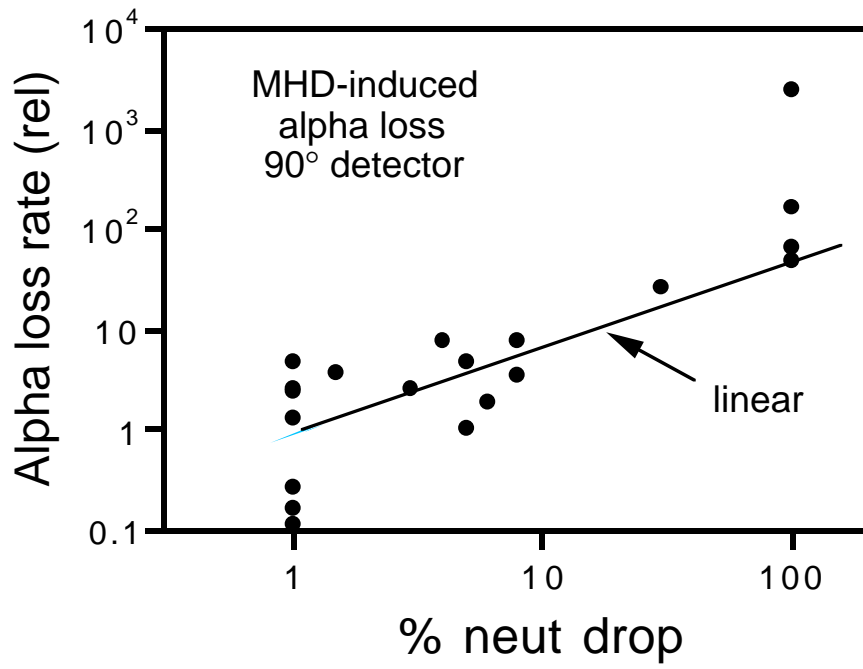


Fig. 15

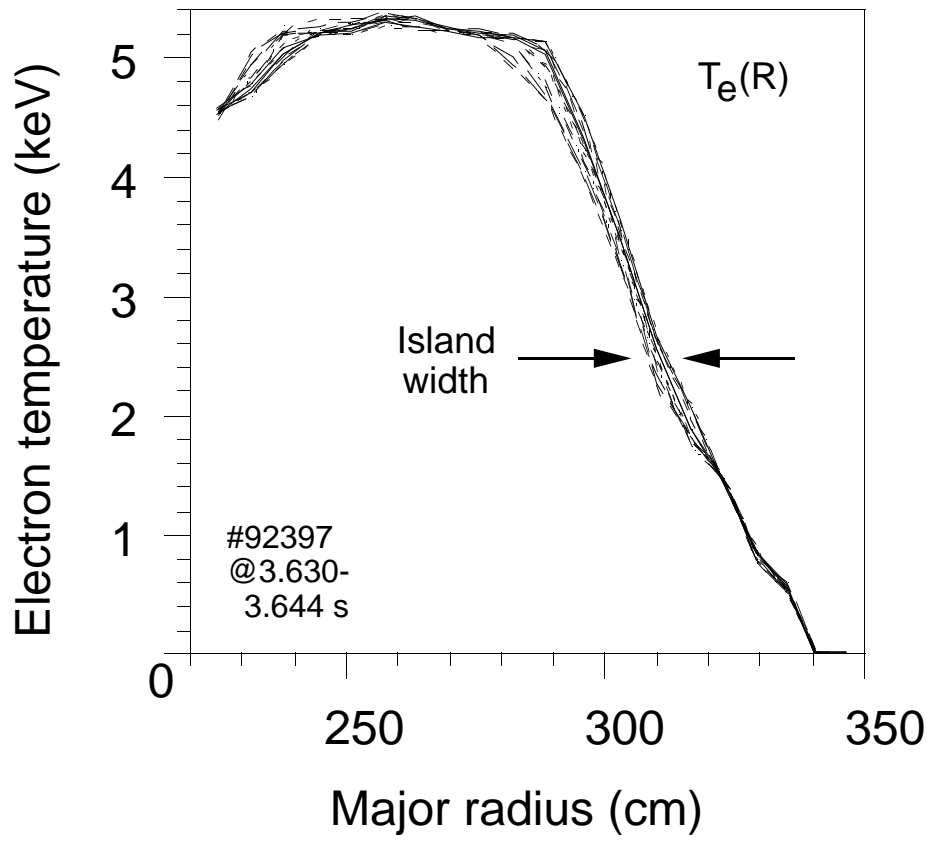


Fig. 16

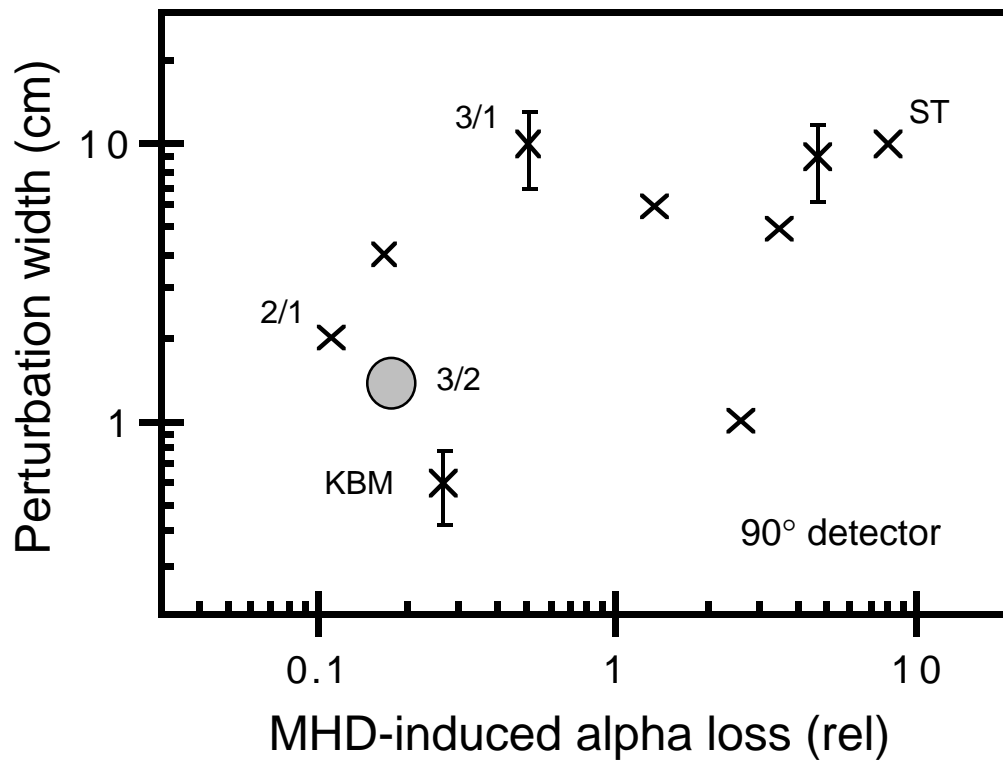


Fig. 17

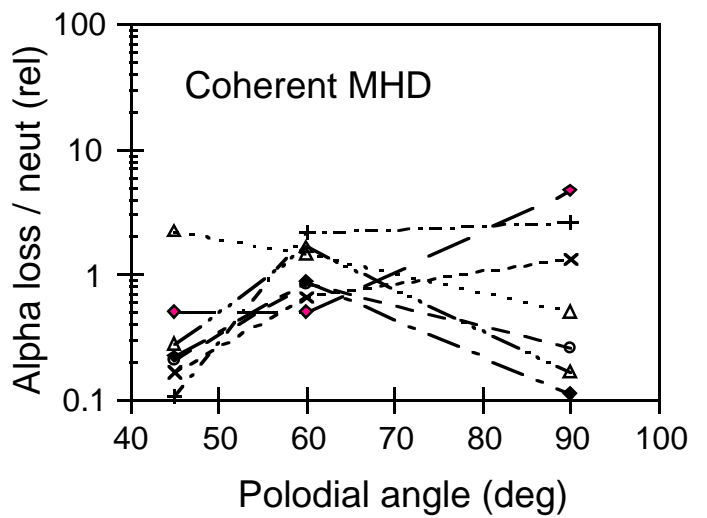
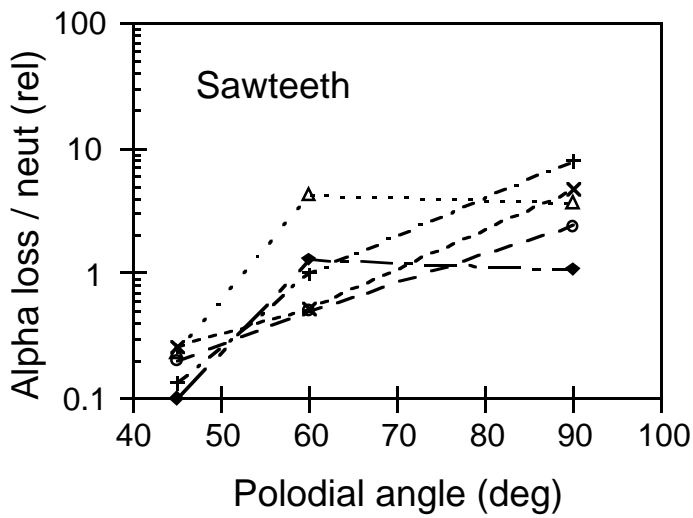
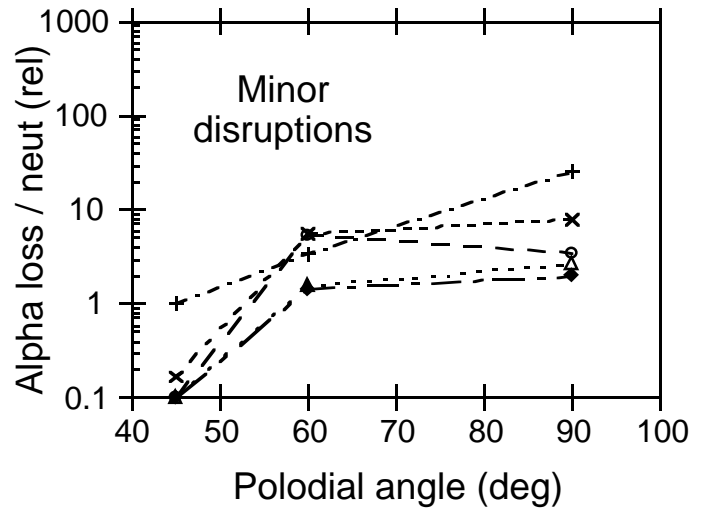
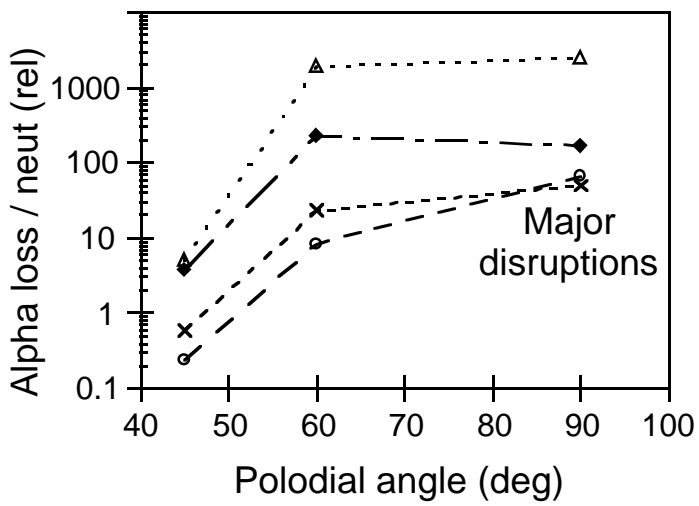


Fig. 18

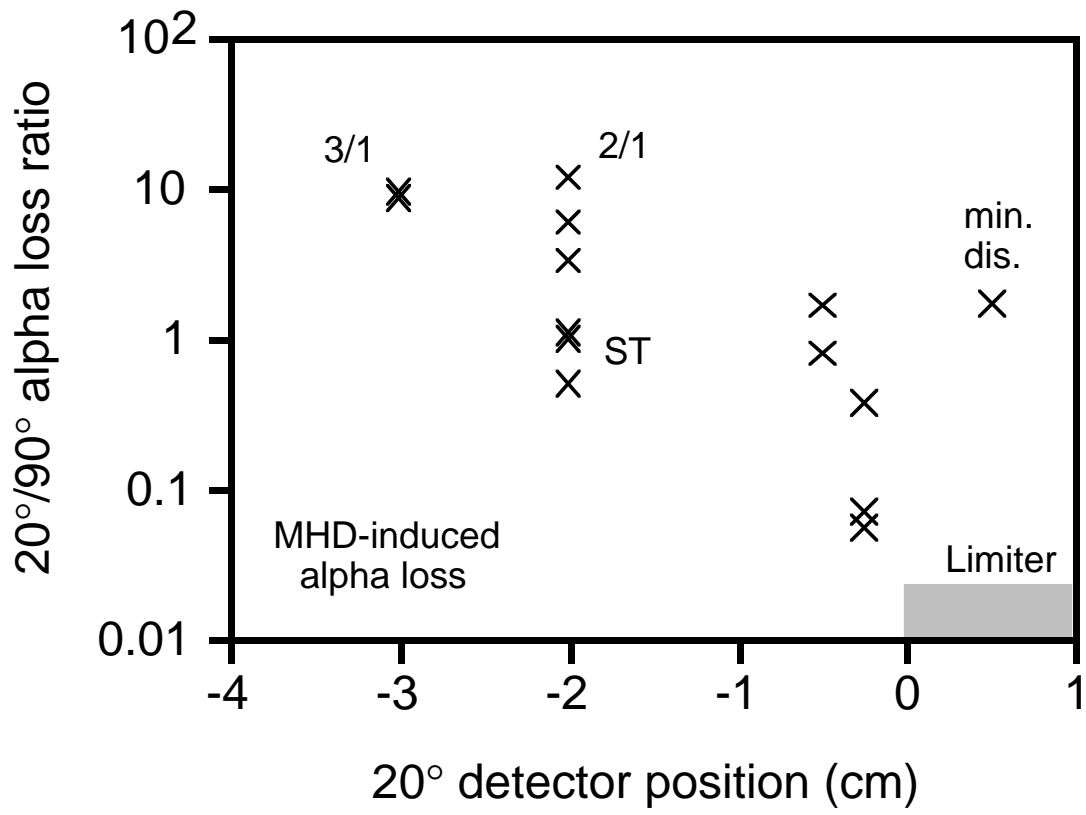


Fig. 19

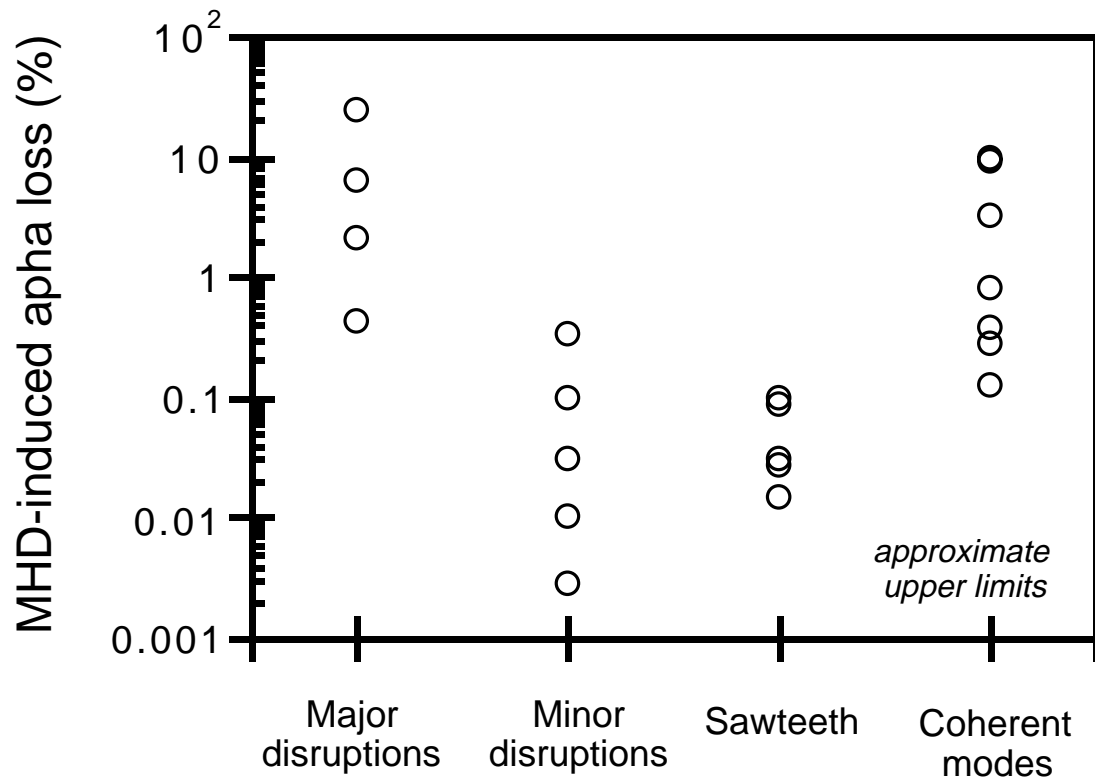


Fig. 20

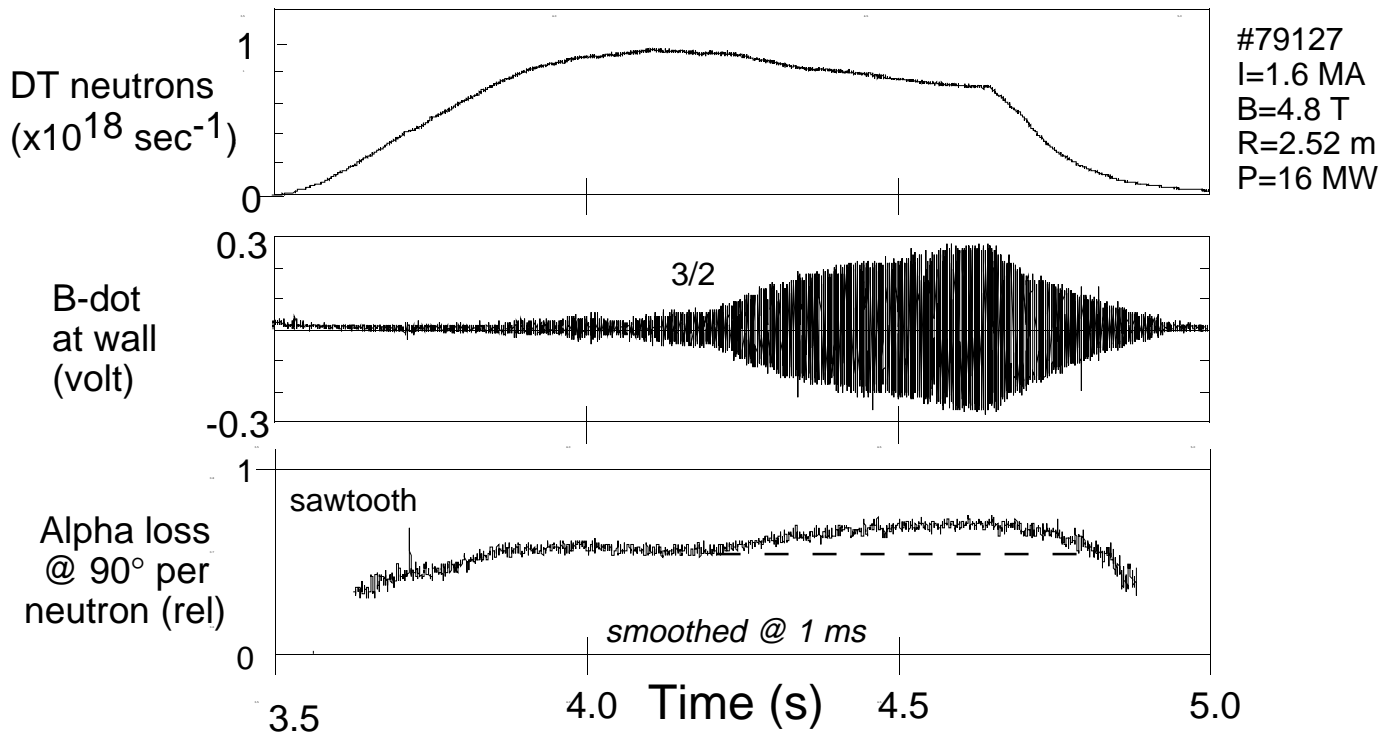


Fig. 21

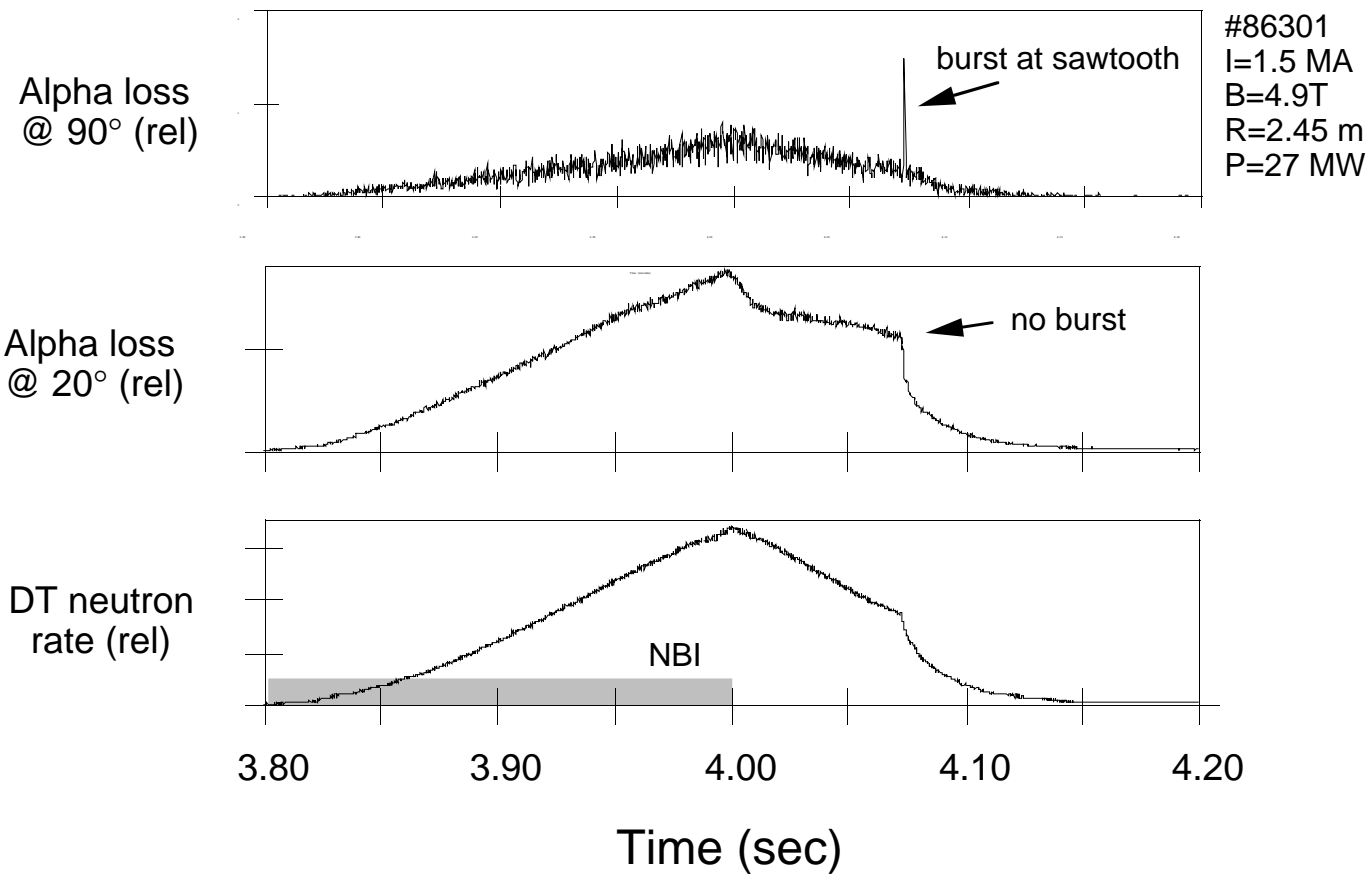


Fig. 22

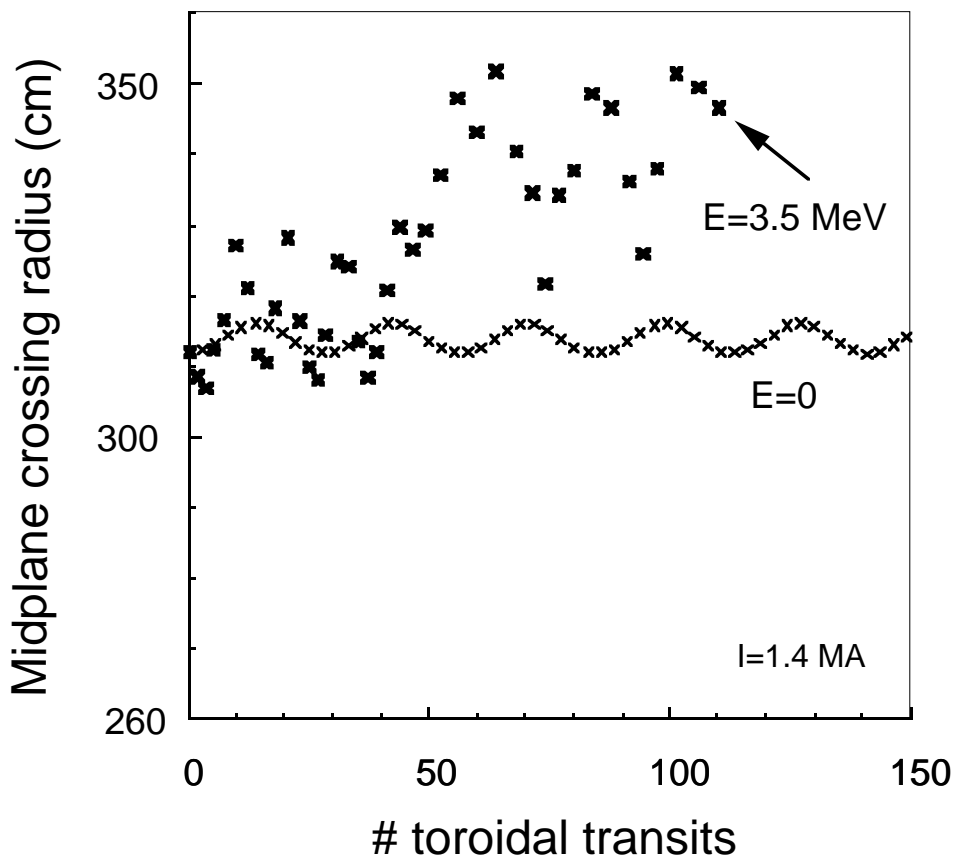
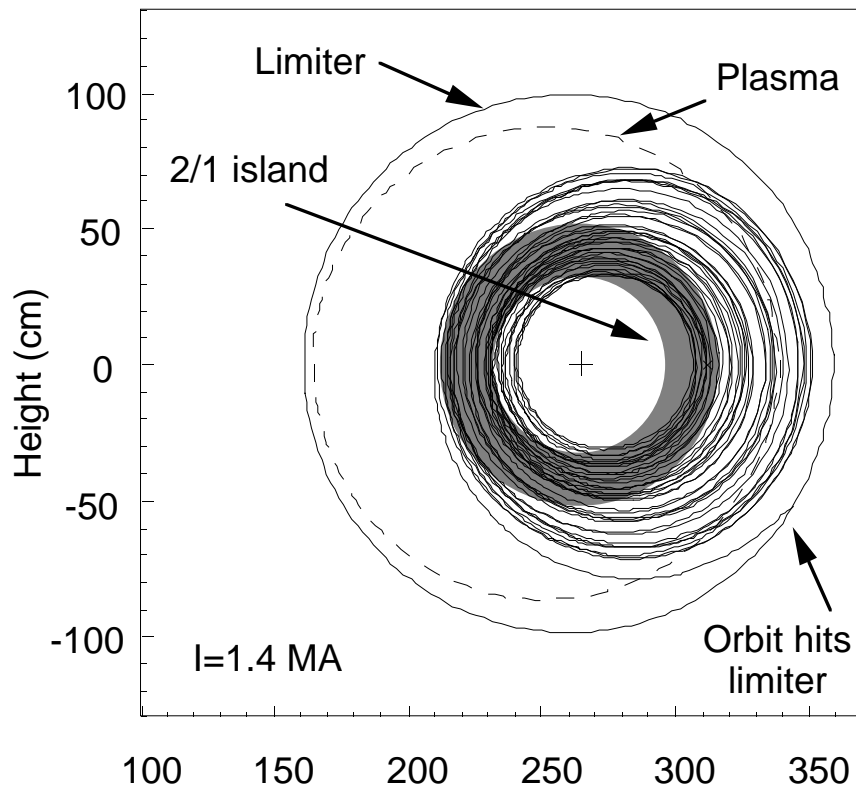


Fig. 23

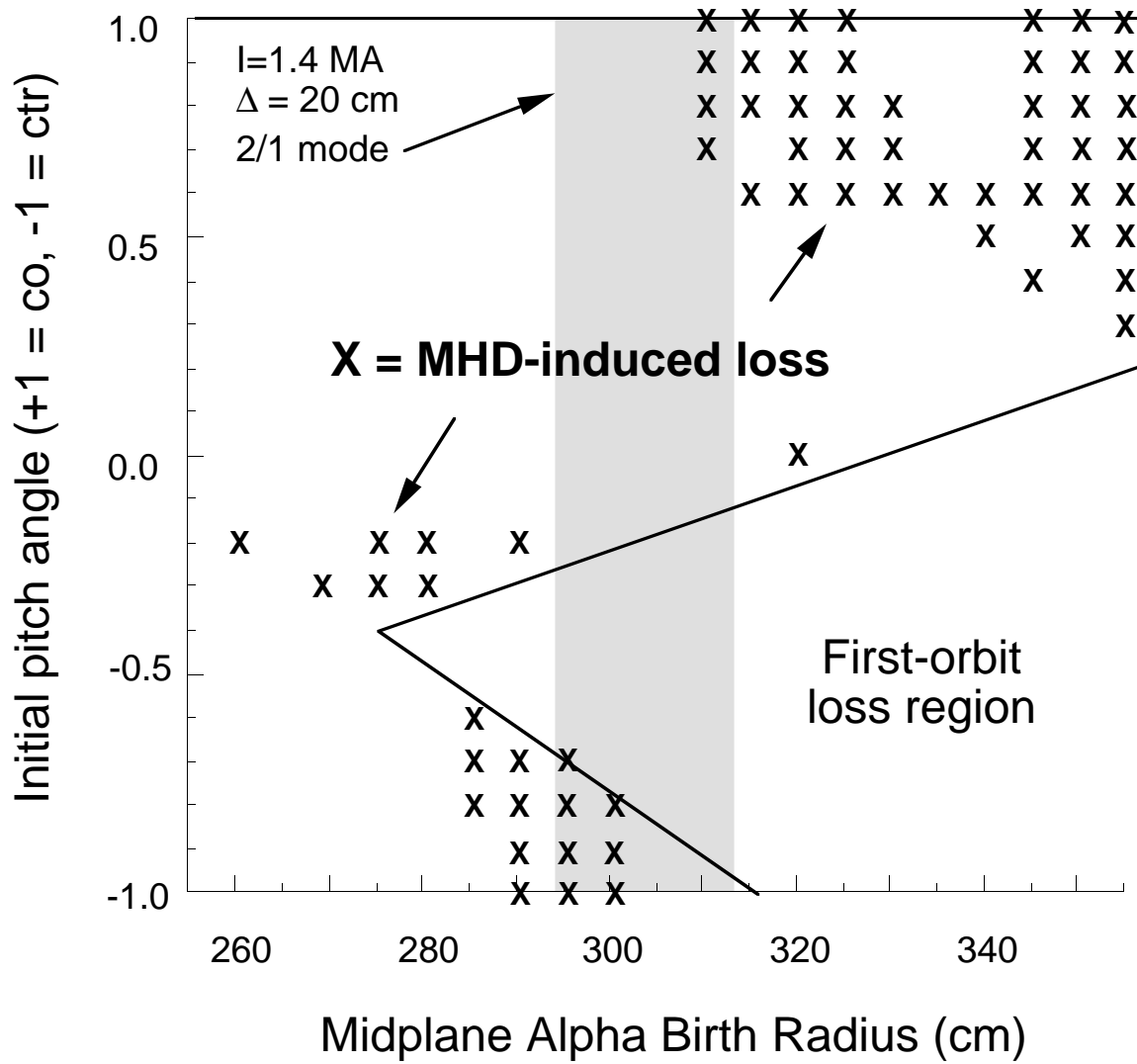


Fig. 24

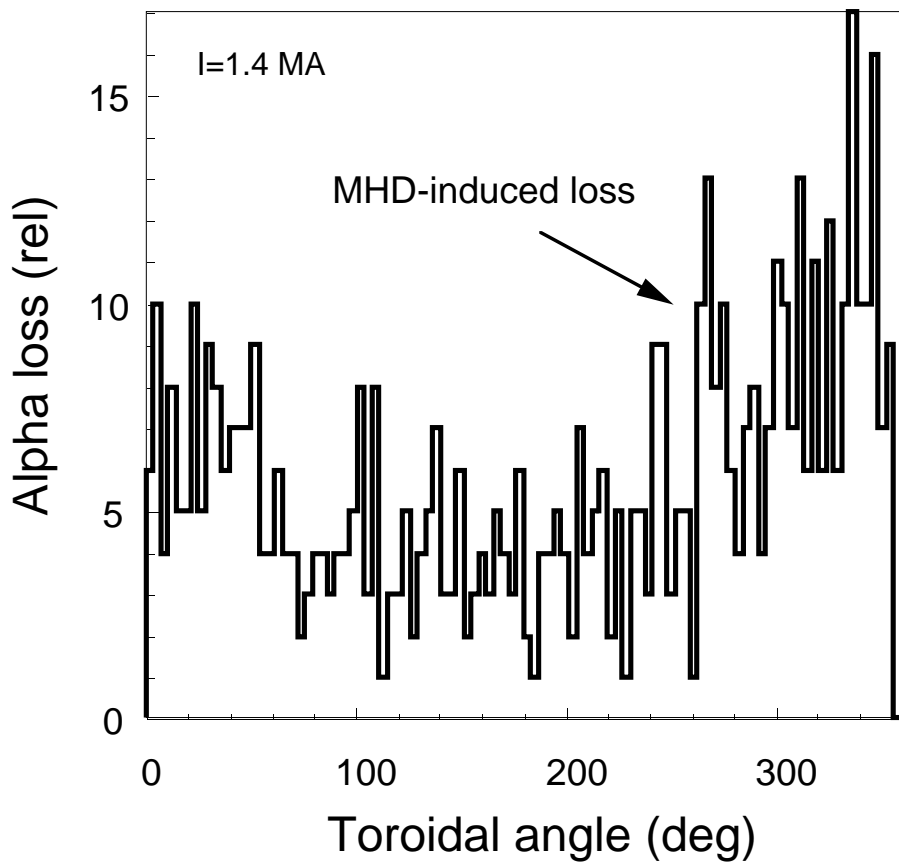
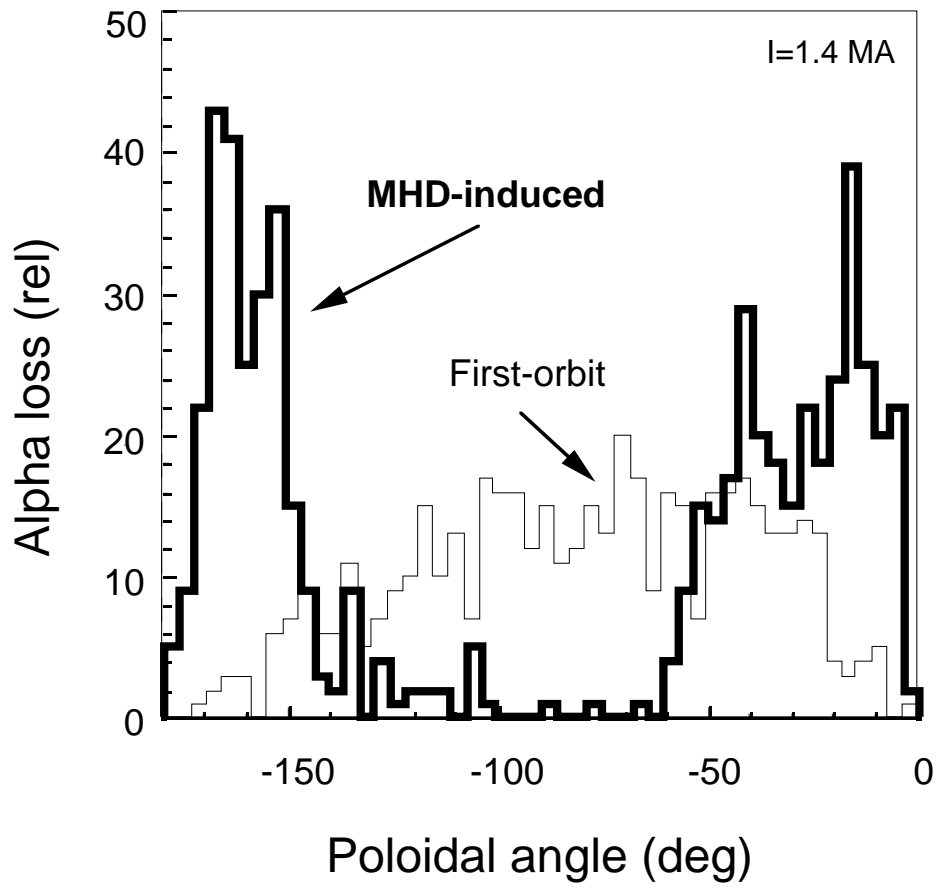


Fig. 25

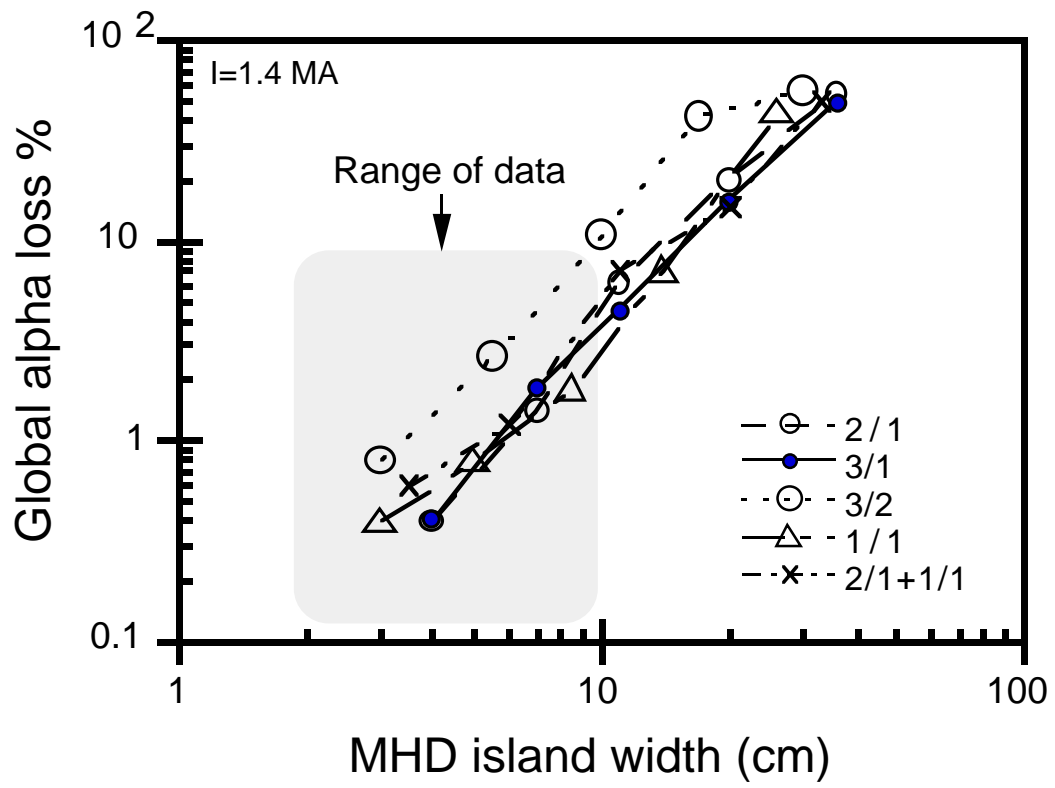


Fig. 26

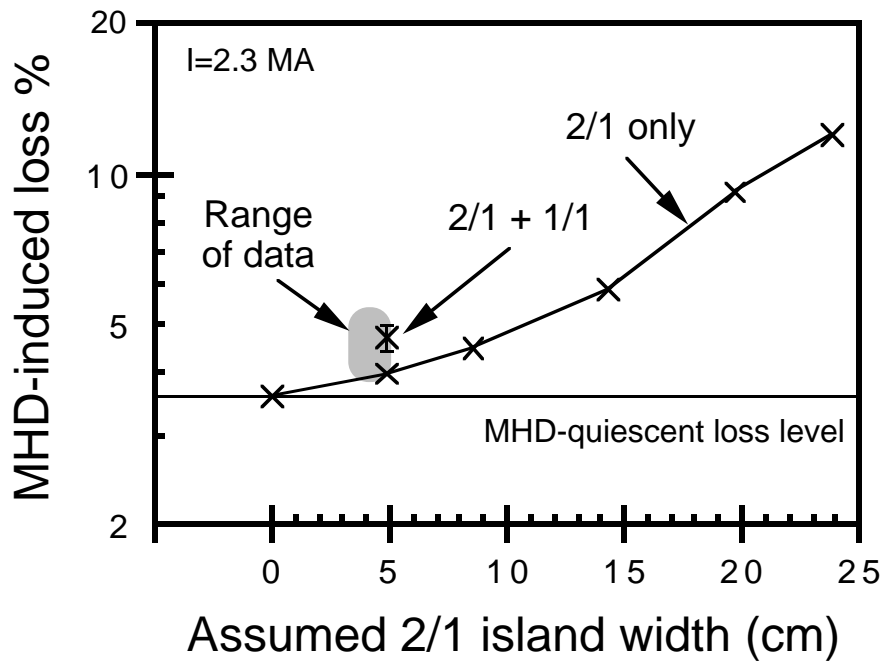


Fig. 27

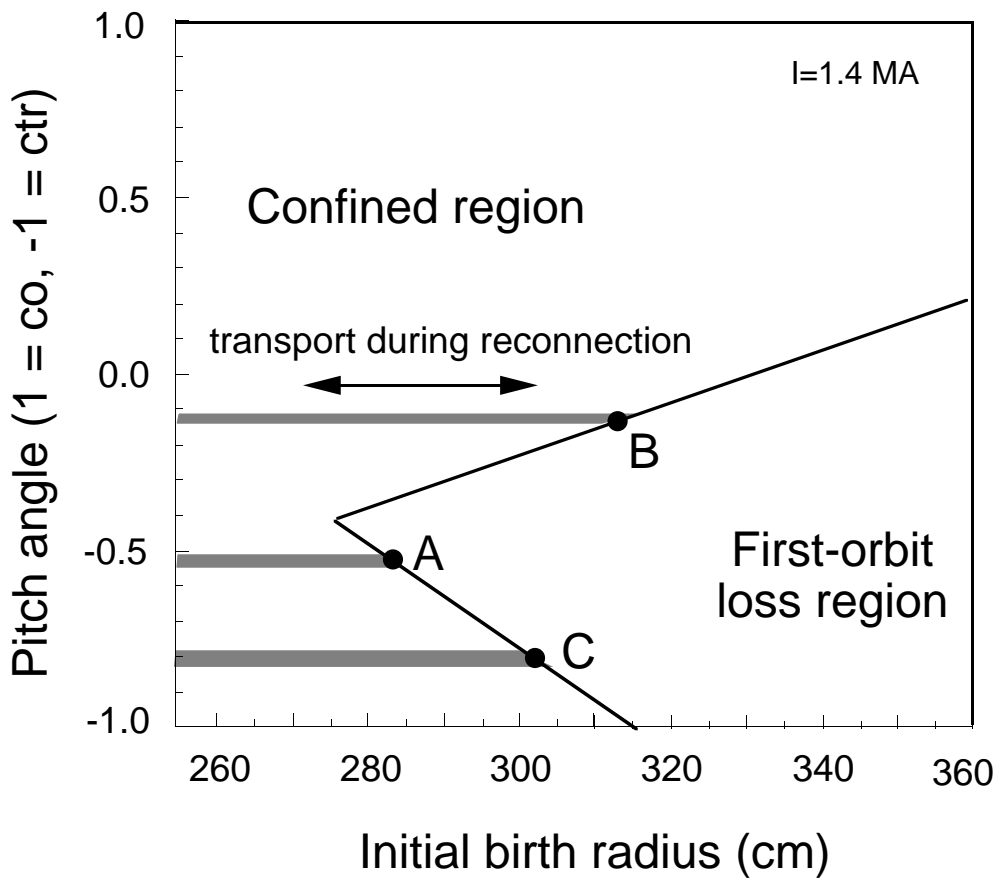
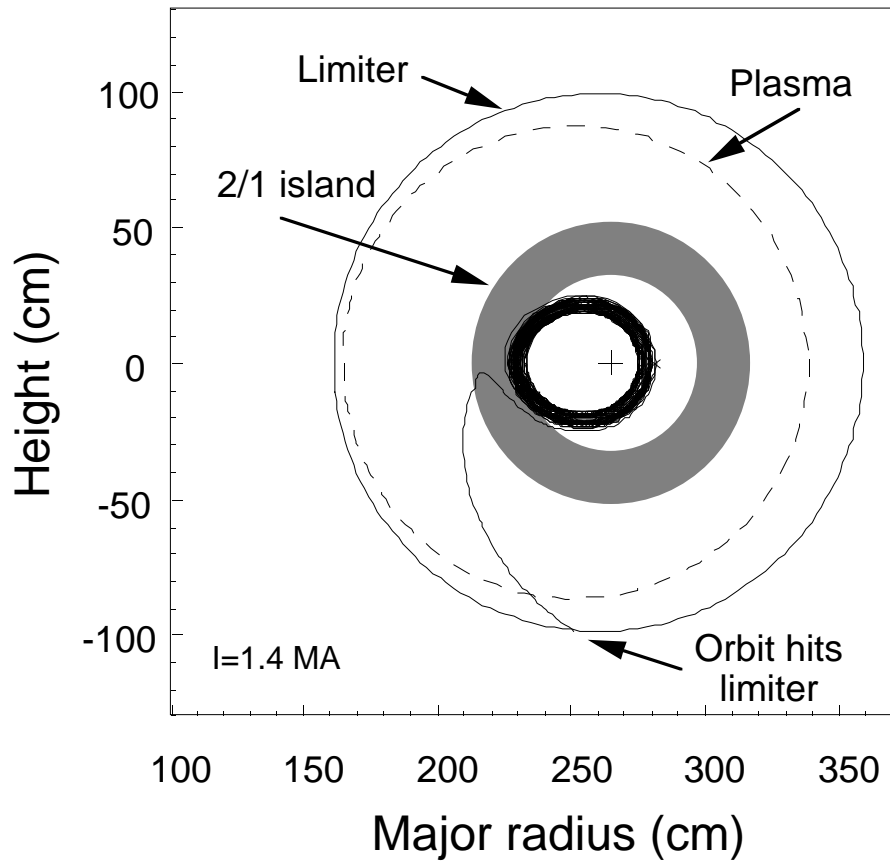


Fig. 28

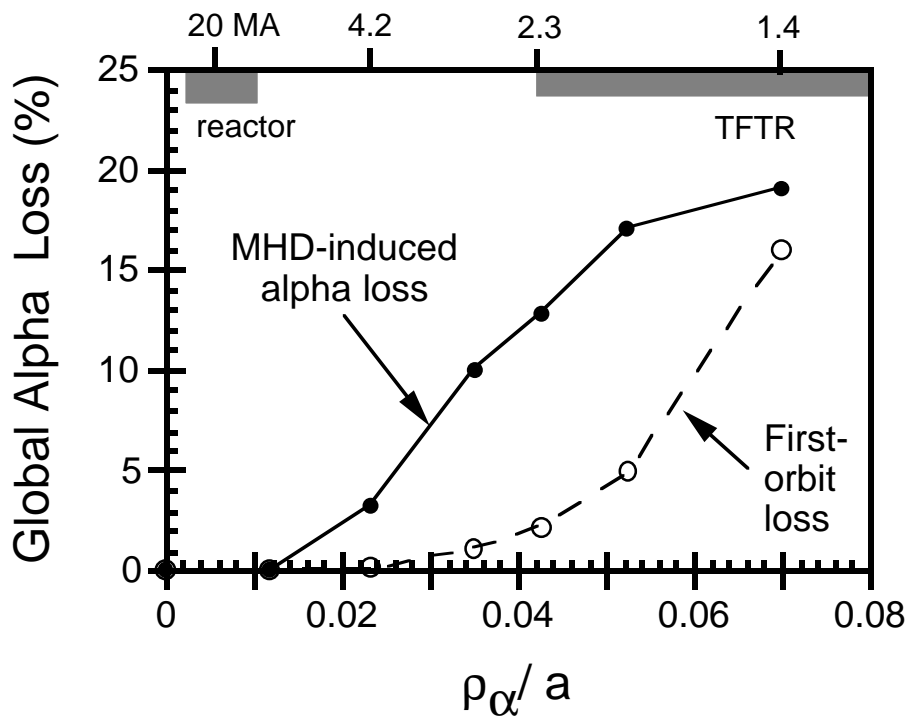
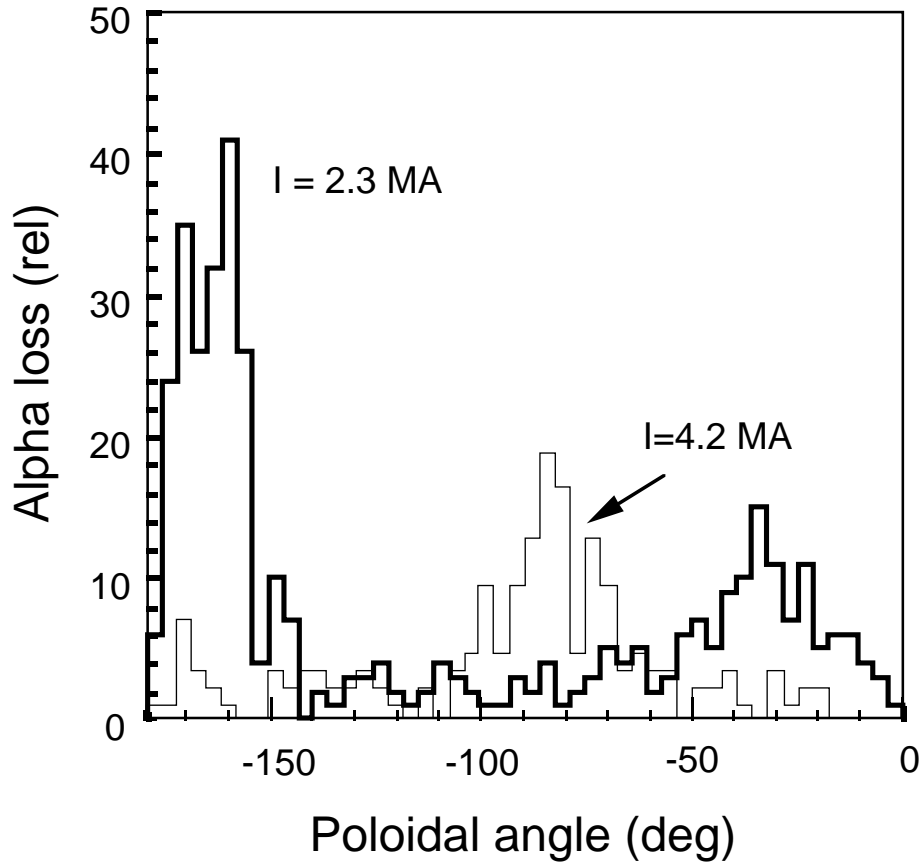


Fig. 29